Title
Development and application of novel fluorescence methods to analyze particle dynamics in cell cytoplasm

Author
Kao, Hung Pin

Publication Date
1994

Peer reviewed|Thesis/dissertation

Development and Application of Novel Fluorescence Methods to Analyze Particle Dynamics in Cell Cytoplasm

by

Hung Pin Kao

DISSERTATION

Submitted in partial satisfaction of the requirements for the degree of

DOCTOR OF PHILOSOPHY

in

Bioengineering

in the

GRADUATE DIVISION

of the

UNIVERSITY OF CALIFORNIA

San Francisco

Dedicated to my parents and to my teachers.

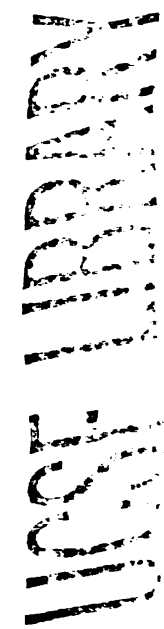

ACKNOWLEDGEMENTS

I regard the time I have spent on this work as the greatest learning experience of my life and I shall always remember the knowledge and experience I have learned over the past five years. I am indebted to my advisor, Dr. Alan S. Verkman, for the support and excellent guidance he has given me throughout my doctoral program. From his example and advice, I have learned to be a better scientist and engineer.

I am indebted to my dear friends, Dr. James R. Abney and Dr. Bethe Scalettar for their assistance and support during the course of my research. Their profound insights changed my opinions on science and my approach to solving scientific problems. For this knowledge and their friendship, I will always be grateful.

I thank those who were with me over the course of my doctoral program for their friendship and support: Greg Sherwin, Cordula Welschbillig Biwersi, Dawn Walters, Bill Raymond, Olivier Seksek, Marion Serfaty, and Barry Tulk. I am especially grateful to Joachim Biwersi, Jay Diamond, and Barbara Herndon, all of whom had a front seat on the roller coaster. All my friends have always been a source of strength to me and I will always remember their kindness.

I thank my family for all the love, support, advice and guidance they have given me. I thank my brother, Hung Teh, my sisters, Hung Mei and Hung Hsueh, and my cousin, Ping Sze, who have always encouraged and supported me. I especially thank my mother, Leatrice, for her love, support, kindness, and encouragement throughout my doctoral program. Lastly and most importantly, I wish to thank my most influential teacher, my father, Kwan Chi, for his love, encouragement, concern, and support for my education both in and out of school. I am thankful for and will always remember the education and happiness he has given me.

The text of chapter 2 of this dissertation is a reprint of the material as it appears in the Journal of Cell Biology. The coauthors listed in this publication directed and supervised the research which forms the basis for this chapter.

The text of chapter 3 of this dissertation is a reprint of the material as it appears in the Biophysical Journal. The coauthor listed in this publication directed and supervised the research which forms the basis for this chapter.

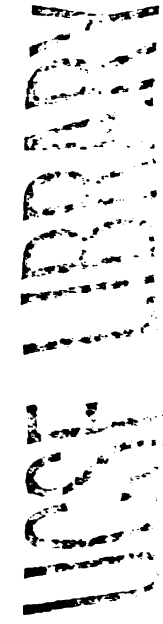

Development and Application of Novel Fluorescence Methods to Analyze Particle Dynamics in Cell Cytoplasm

by

H. Pin Kao

Biochemical reaction rates in the cytoplasm are influenced by reactant diffusion. The goals of this thesis were to determine the factors which influence the cytoplasmic translational diffusion of metabolite-sized molecules and to develop new technology to measure the diffusion of fluorescent particles in cells. There are 3 main projects: 1) The first measurement and quantitative analysis of the translational mobility of a small solute in cell cytoplasm was made using fluorescence recovery after photobleaching (FRAP). The factors which influence the translational diffusion of a metabolite-sized fluorescent molecule, 2,7-bis-(2-carboxyethyl)-5-(and 6-)carboxyfluorescein (BCECF), in the cytoplasm of Swiss 3T3 fibroblasts were evaluated by comparing translational and rotational diffusion in cytoplasm, dextran solutions and agarose gels. BCECF translational diffusion was hindered by 3 independent factors: *(a) fluid-phase cytoplasmic viscosity* reduced diffusion by 22 %, *(b) binding to intracellular components* reduced diffusion by 19 %, and *(c) collisions with cell solids* reduced diffusion by 60 %. Together, these factors predict an ≈ 75 % reduction of translational diffusion compared to that in water, in agreement with the measured reduction of ≈ 73 %. 2) The first nanometer-resolution, three-dimensional single particle tracking technique was developed. A cylindrical lens in the detection optics of an epifluorescence microscope produced images which encoded the particle's x,y,z position. Spatial resolution was 12 nm (SD) along the optical axis and 5 nm in the image plane with a maximum sampling rate of ≈ 4 Hz. This technique was applied to track fluorescent beads in artificial solutions and living cells. 3) A FRAP apparatus was constructed to measure fluorescence recovery half-times down to 200 μs. Photobleaching pulses were formed with a minimum width of ≈ 6 μs and fluorescence signals were detected using a photomultiplier and transimpedance amplifier. A circuit was

designed to gate the photomultiplier off during the photobleaching pulse to prevent photodamage and overload. This apparatus was used to measure the fluorescence recoveries of fluorescein dextran solutions. The new measurement methods and theoretical analyses of solute diffusion presented here should be useful in further analyses of intracellular component mobility in living cells.

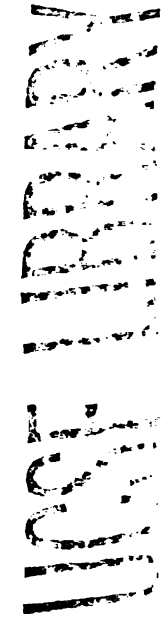

TABLE OF CONTENTS

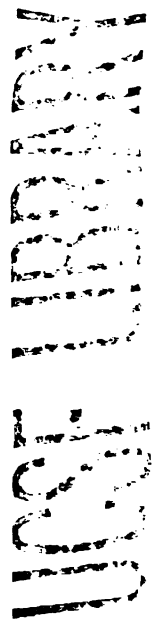

LIST OF ILLUSTRATIONS

Chapter 1

INTRODUCTION

Cell cytoplasm is composed of organelles suspended in a mixture of solutes and macromolecules, all of which are organized within a network of filamentous proteins known as the cytomatrix. Within this crowded milieu, protein synthesis and metabolic processes vital to the function of the cell occur. The biochemical rates and equilibria of these processes are strongly influenced by the cytoplasmic environment. A cytoplasmic characteristic which is often overlooked in investigations of biochemical reactions is the interaction of the reactants and products with other macromolecular species. Such interactions can strongly influence the rates of biochemical reactions through changes in the diffusability of the reactants and non-specific binding (Zimmerman and Minton, 1993). The focus of this thesis was to determine the factors which influence the translational diffusion of metabolite-sized molecules in the cytoplasm and to develop new technology for the measurement of the diffusion of fluorescent particles in cells. Further details about relevant previous works in the field and the experimental rationale are provided in chapters 2 to 4.

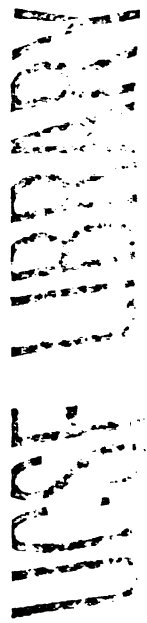

Several factors related to the structure of the cytoplasm decrease the translational diffusion of a molecule in the cytoplasm relative to that in water. The relative contribution of each factor to the diffusional motion depends upon the size of the diffusing molecule and the distance over which the diffusion is measured. Most studies have focused on only the diffusion of large macromolecules over long distances (>2 μm) in the cytoplasm and have not attempted to analyze quantitatively the factors which affect this diffusion. To date, there has been no exact measurement of the diffusion of small metabolite-sized molecules

(e.g., glucose, ATP and amino acids) in cytoplasm. In chapter 2, the first measurement and quantitative analysis of the translational diffusion of a small molecule over long distances in cell cytoplasm is presented. Fluorescence recovery after photobleaching was used to measure and compare the translational diffusion of small molecules in cell cytoplasm and in artificial solutions; data analysis methods were developed for the quantitative determination and evaluation of the translational mobility in cell cytoplasm.

In the cytoplasm, the diffusion of molecules over short (< 1 μm) and long distances are expected to differ as a result of the sieving properties of the cytomatrix. In plasma membranes, this sieving property has been observed using two-dimensional single particle tracking (SPT). However, to date, no analogous study has been performed in the cell cytoplasm because SPT has only been developed for two dimensional systems. In chapter 3, the development of the first three-dimensional SPT apparatus is presented. This apparatus optically measured the trajectory of single fluorescent particles at nanometer resolution in real time. The technique is simple to implement and its principle is applicable to the types of microscopy which are used in conventional two-dimensional SPT studies. The speed and accuracy of this apparatus are limited only by the rate at which images of the particle can be collected and the signal to noise ratio of these images. Applications of three-dimensional SPT in model and biological specimens are presented.

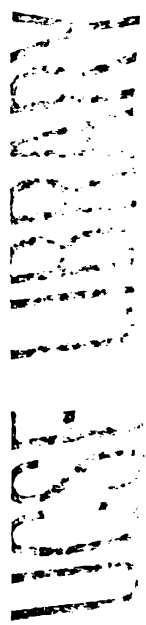

For fluorescence recovery after photobleaching experiments, the half-time of the fluorescence recovery is related to the size of the probed region and the fluorescent molecule. In studies involving small probed regions or small fluorescent molecules, very rapid fluorescence recoveries (< 1 ms) are expected, as expected for measurements in cellular organelles or at the plasma membrane-cytoplasm interface. In chapter 4, a fluorescence recovery after photobleaching apparatus was constructed and evaluated to measure fluorescence recoveries down to 200 μs. This half-time is theoretically expected for a photobleaching recovery experiment using a beam width of 1 μm (the spot size of a 1

Chapter 2

DETERMINANTS OF THE TRANSLATIONAL MOBILITY OF A SMALL SOLUTE IN CELL CYTOPLASM

2.1 Summary

The purposes of this study were: (a) to measure the translational mobility of a small solute in cell cytoplasm; (b) to define quantitatively the factors that determine solute translation; and (c) to compare and contrast solute rotation and translation. A small fluorescent probe, 2,7-bis-(2-carboxyethyl)-5-(and 6-)carboxyfluorescein (BCECF), was introduced into the cytoplasm of Swiss 3T3 fibroblasts. BCECF translation was measured by fluorescence recovery after photobleaching; rotation was measured by Fourier transform polarization microscopy. Diffusion coefficients relative to those in water (D/D_0) were determined by comparing mobility in cytoplasm with mobility in standard solutions of known viscosity. At isosmotic cell volume, the relative diffusion coefficients for BCECF translation and rotation in cytoplasm were 0.27 ± 0.01 (SEM, n=24, 23° C) and 0.78 ± 0.03 (n=4), respectively. As cell volume increased from 0.33 to 2 times isosmotic volume, the relative translational diffusion coefficient increased from 0.047 to 0.32, while the relative rotational diffusion coefficient remained constant. The factors determining BCECF translation were evaluated by comparing rotation and translation in cytoplasm, and in artificial solutions containing dextrans (mobile barriers) and agarose gels (immobile barriers). It was concluded that the hindrance of BCECF translation in cytoplasm could be quantitatively attributed to 3 independent factors: *(a)* fluid-phase cytoplasmic viscosity is 28% greater than the viscosity of water (factor 1 = 0.78), *(b)* 19% of BCECF is transiently bound to intracellular components of low mobility (factor 2 = 0.81), and most importantly,

(c) translation of unbound BCECF is hindered 2.5-fold by collisions with cell solids comprising 13 % of isosmotic cell volume (factor 3 = 0.40). The product of the 3 factors is 0.25 ± 0.03, in good agreement with the measured D/D_0 of 0.27 ± 0.01. These results provide the first measurement of the translational mobility of a small solute in cell cytoplasm and define quantitatively the factors that slow solute translation.

2.2 Introduction

Cell cytoplasm is a complex non-Newtonian fluid comprising an aqueous fluid-phase filling the space within an entangled mesh of filamentous skeletal proteins (cytomatrix) and other macromolecular structures (Bridgman and Reese, 1984; Clegg, 1984; Fulton, 1982; Gershon et al, 1985; Keith, 1973; Mastro and Keith, 1984; Porter, 1984). The factors that determine the rotation and translation of solute molecules within this crowded milieu have been the topic of considerable recent interest due to their probable impact on the rates of metabolic reactions. At least three cytoplasmic factors will contribute to solute mobility: *(a)* fluid-phase cytoplasmic viscosity, i.e., the viscosity in the aqueous space between macromolecules, *(b)* solute binding to macromolecular structures, and *(c)* collisional (direct plus hydrodynamic) interactions between the solute and macromolecular obstacles. The relative contributions of these three factors will depend on solute size and the type and extent of solute motion. In this study we focus primarily on the long (relative to the characteristic macromolecular spacing) range translation of small solutes. Such motion plays a role in many cellular processes, including the translocation of cyclic nucleotides in signal transduction, the vectorial transport of solutes across epithelial cells, and the movement of nucleic acids from the cytoplasm to the nucleus for replication and transcription. The translational diffusion of a small solute in cell cytoplasm has not been measured previously by fluorescence recovery after photobleaching (FRAP).

Most studies of dynamics in the cytoplasm have focused on measurement of a

single parameter that reflects how rapidly molecules rotate or translate. These measurements thus yield "apparent" cytoplasmic viscosities, which reflect all impediments to motion: the true fluid-phase viscosity, the effects of binding, and the effects of collisions. When the rotational mobility of small molecules in the cytoplasm is characterized in this fashion using electron spin resonance (Keith et al, 1977; Lepock et al, 1983; Mastro et al, 1984) or steady-state fluorescence anisotropy techniques (Dix and Verkman, 1990; Lindmo and Steen, 1977), apparent rotational viscosities in the range 2 to 20 cP (water is 1 cP) are obtained. Similarly, when translational mobilities are characterized via direct observation of the diffusion of microinjected dyes, electron spin resonance, or FRAP, apparent translational viscosities are found to lie in the same range (Jacobson and Wojcieszyn, 1984; Kreis et al., 1982; Luby-Phelps et al, 1986; 1987; 1988; Wojcieszyn et al, 1981). The interpretation of these values is subject to several caveats. First, the electron spin resonance results are based on an uncertain estimate of intracellular probe concentration, while the FRAP results are based on an extrapolation of data obtained from probes of different molecular size to zero size. Second, and more importantly, none of these results provide quantitative information about the individual factors contributing to the measured viscosity.

We recently introduced a method of determining fluid-phase viscosity (microfluorimetric measurement of picosecond anisotropy decay; Fushimi and Verkman, 1991) that overcomes many of the limitations in previous measurements of solute mobility in cells. The data yield the rotational mobilities of bound and unbound probe, as well as the fraction of probe in each state. These measurements revealed that a significant (15% - 30%) fraction of fluorophores bind to relatively immobile cellular components. More importantly, they demonstrated that the fluid-phase cytoplasmic viscosity sensed by the unbound probe was in the range 1.2-1.4 cP for several small fluorophores in Swiss 3T3 fibroblasts (Fushimi and Verkman, 1991) and several types of kidney epithelial cells (Periasamy et al, 1992). This is a surprisingly low viscosity, suggesting that the physical

properties of aqueous domain cell cytoplasm are similar to those of water.

The purposes of the present study are: *(a)* to measure the translational mobility of a small solute in cell cytoplasm, *(b)* to define quantitatively the factors that determine solute translational mobility, and *(c)* to compare and contrast the rotation and translation of probes in the cytoplasm. A FRAP apparatus was constructed and data analysis methods were developed for quantitative determination of the translational mobilities of small molecules that diffuse rapidly in cell cytoplasm. It was found that the translational diffusion of a small fluorescent probe was approximately four times slower in cell cytoplasm than in water. It is shown that this inhibition of translational diffusion arises because fluid-phase cytoplasmic viscosity is slightly higher than the viscosity of water, a small amount of probe binds to intracellular structures, and, most significantly, because the probe collides with intracellular structures.

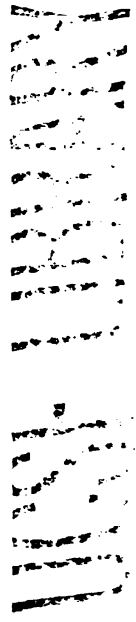

2.3 Materials and Methods

Cell culture and labeling

Swiss 3T3 fibroblasts (American Type Collection No. CL-101, Rockville, MD) were grown on 18-mm diameter round glass coverslips in DME-H21 supplemented with 5 % fetal calf serum, 100 U/ml penicillin and 100 mg/ml streptomycin. Cells were maintained at 37° C in a 95 % air / 5 % CO_2 incubator and used before cells had attained confluence. Cells were labeled with 2,7-bis-(2-carboxyethyl)-5-(and 6-)carboxyfluorescein (BCECF) by a 10 min incubation with 5 μM BCECF-AM (acetoxylmethylester, Molecular Probes, Junction City, OR) at 37° C in phosphate-buffered saline (PBS: 138 mM NaCl, 2.7 mM KCl, 0.7 mM $CaCl_2$, 1.1 mM $MgCl_2$, 1.5 mM KH_2PO_4, 8.1 mM Na_2HPO_4, 5 mM glucose, pH 7.4). Cells were then washed and incubated for an additional 15-30 min at 37° C in buffer not containing BCECF-AM to facilitate intracellular deesterification. Coverglasses containing BCECF-loaded cells were transferred to a 200-

μL perfusion chamber (to facilitate buffer changes) in which the cell-free surface of the coverglass was accessible to a nonimmersion objective or a short-working-distance immersion objective (Chao et al, 1989). All experiments were carried out at 23° C.

FRAP apparatus

A FRAP apparatus was constructed to resolve recovery half-times down to 5 ms (Fig. 2.1). Cells were illuminated with a Gaussian-profile beam (488 nm) from a CR-4 Ar laser (Coherent, Sunnyvale, CA) focused to a 3 μm radius spot through a 16X quartz objective (Leitz, numerical aperture 0.25) on an inverted epifluorescence microscope. To photobleach the sample, an unattenuated laser pulse (4-5 x 10^3 times more intense than the probe beam) of 2-3 ms duration was generated using a rapid shutter (Uniblitz, model T132, Vincent Associates, Rochester, NY). To monitor prebleach and postbleach fluorescence, an attenuated probe beam was formed by reflections off of two glass wedge prisms and two front-surfaced mirrors; a neutral density filter (1.8 O.D. units) was positioned between the mirrors to set the attenuation ratio. The mirrors and wedge prisms were mounted on two-axis micropositioners to facilitate alignment of the unattenuated and attenuated beams. Emitted fluorescence passed through a 510-nm dichroic mirror, GG515 barrier filter, and rapid shutter (to protect the photomultiplier during the photobleaching pulse; Uniblitz, model D122), and was detected by an R928 photomultiplier (Hamamatsu, Middlesex, NJ) operating at 500-900 volts. Photomultiplier signals were amplified (Model 110F, Pacific Instruments, Concord, CA; response time < 0.1 ms) and digitized by a 12-bit analog-to-digital converter (Lab Master, Scientific Solutions, Solon, OH) interfaced to a 386 cpu. During each experiment, the first 3000 data points were collected at a rate of 100 μs - 1 ms per point, while the remaining 1700 - 1930 data points were collected at a rate of 10 ms per point.

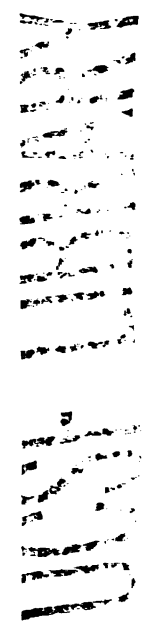

Figure 2.1. Schematic of FRAP apparatus designed to measure recovery times down to 5 ms. See Materials and Methods section for details.

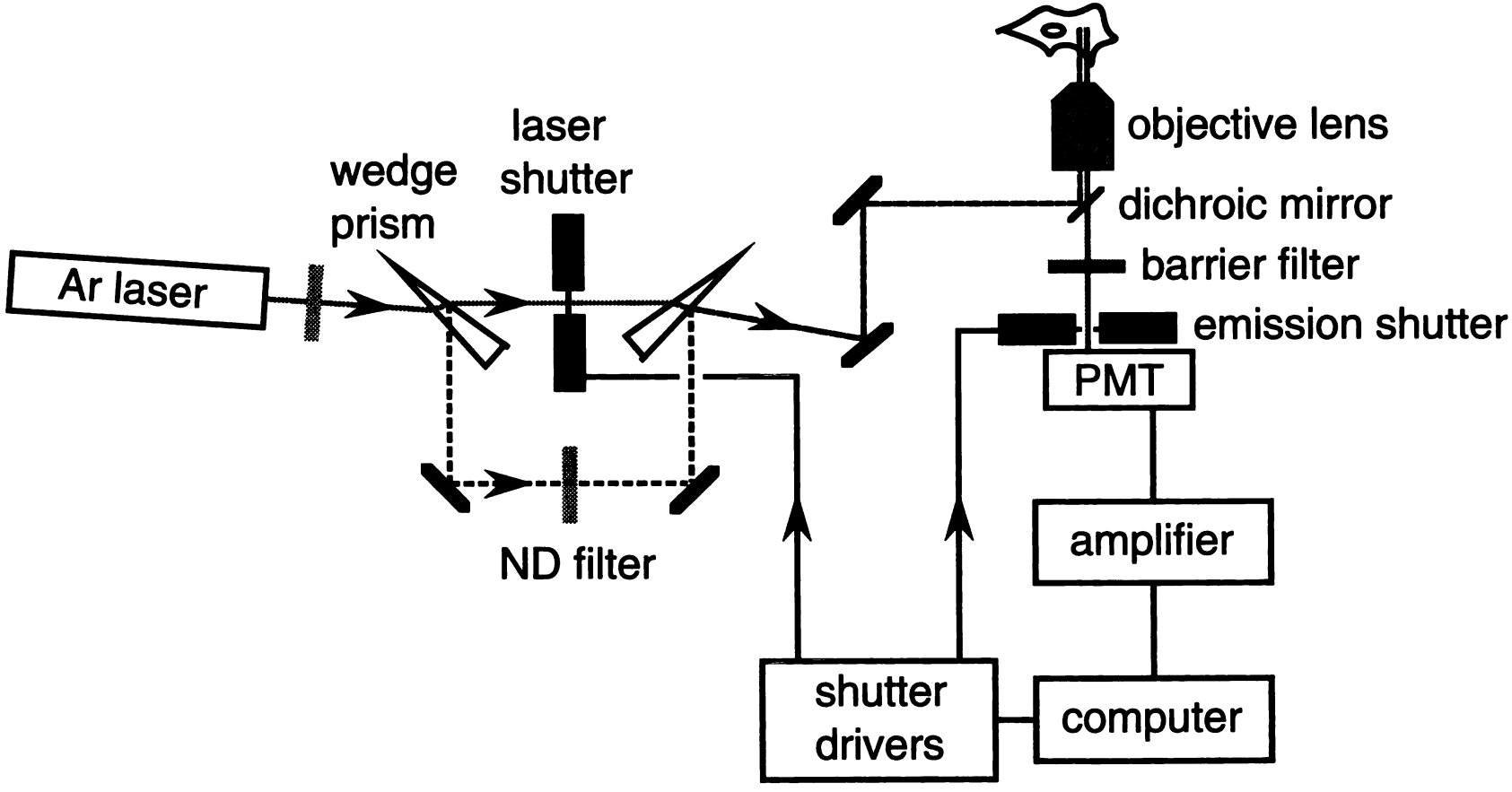

FRAP experimental procedures and data analysis

Before each set of experiments, the FRAP instrument was stabilized for 90 min, and the attenuated and unattenuated beams were aligned and steered along the optical axis of the microscope. The recovery curves for a series of 5 to 8 calibration solutions were measured in quadruplicate before and after every set of experiments to provide an internal standard and to ensure that beam drift did not occur. The calibration solutions, which consisted of 0.1 μM BCECF in PBS (pH 7.4) containing sucrose (0-540 g/L), yielded macroscopic viscosities of 1.02 to 23.2 cP as measured by a Cannon-Fenske viscometer (models 50 and 100, Cannon Instru. Co., State College, PA); measured viscosities were in close agreement with data in the CRC handbook (Weast, 1986). FRAP measurements were performed on calibration solutions of 2 - 50 μm thickness prepared by depositing a defined μL volume of solution between an 18-mm diameter round coverglass (above) and a larger rectangular coverglass (below). The solution spread evenly within the area of the round coverglass. Film thickness was confirmed from the z-axis translation required to focus on the upper and lower solution/glass interfaces.

Photobleaching parameters were computed as follows. In each measurement, the prebleach fluorescence, F(-), was determined from the average fluorescence over a 1 s interval prior to photobleaching. The time course of fluorescence recovery after photobleaching, F(t), was described by a 4-parameter biexponential function, $F(t) = A_1 \exp(-t/\tau_1) + A_2 \exp(-t/\tau_2) + F(\infty)$, where $\tau_1 < \tau_2$. $F(\infty)$ is the (constant) fluorescence at long times after photobleaching and was determined from the average of F(t) over a 5 s interval 15-20 s after the photobleaching pulse. The F(t) curve was fitted by the successive integration procedure (On-Line Instrument Systems Inc., Jefferson, GA) for t between 7 ms after the end of the photobleaching pulse (well after the emission path shutter was opened) and 100-1000 ms. The fluorescence immediately after bleaching, F(0), was determined by extrapolating F(t) back to zero time. The percent photobleaching was thus equal to 1-F(0)/F(-); the percent recovery was equal to [F(∞)-F(0)] / [F(-)-F(0)]; and the

half-time for recovery, $\tau_{1/2}$, was determined by numerically solving the equation $F(\tau_{1/2}) = [F(\infty)-F(0)]/2$. In ~10 % of the FRAP studies in cells, there was a slow increase in F(t) after recovery possibly due to continued intracellular deesterification of BCECF-AM; in these experiments, F(t) was corrected using the measured rate of fluorescence increase determined from the slope of F(t) vs. t for t between 15 and 20 s.

Apparent viscosities in a given sample were determined by comparison of $\tau_{1/2}$ values for fluorescence recovery after photobleaching in the sample with $\tau_{1/2}$ values for the calibration solutions. The rationale and justification for this approach are discussed below. The diffusion coefficient in the given sample relative to that in water, D/D_0, was then computed as the inverse of the apparent viscosity.

Picosecond anisotropy measurements

Time-resolved fluorescence polarization measurements were carried out by Fourier transform frequency-domain fluorimetry (Verkman et al, 1991). Light from a CR-4 Ar laser was impulse modulated by a Pockels cell and components of an SLM 48000 multiharmonic fluorimeter (SLM Instruments, Urbana IL) to give a 6 MHz series of 1-2 nanosecond pulses of plane-polarized light. ~4% of the light was split to a reference photomultiplier, while the main beam was steered into an inverted epifluorescence microscope and reflected by a 510-nm dichroic mirror for sample excitation through a 40X quartz objective (glycerol immersion, Leitz, numerical aperture 0.65). The beam diameter at the focal plane could be set between 1 μm and ~25 μm. Emitted fluorescence passed through the dichroic mirror, a GG530 barrier filter (Schott Glass, Duryea, PA), and a Glan-Thompson calcite polarizer that could be rotated through 90°. Polarizer alignment, G-factor corrections, and calibration with standards were carried out as described previously (Dix and Verkman, 1990; Fushimi et al, 1990). Differential phase angles and modulation ratios were measured at 35-40 discrete harmonics of the 6 MHz repetition frequency by cross-correlation multi-harmonic detection. The fluorescence from unlabeled

cells was < 2 % of that from BCECF-loaded cells. Phase and modulation data were fitted by a non-linear least-squares procedure (Calafut et al, 1989) to a two-component anisotropy-decay model, $r(t) = g_1 \exp(-t/\tau_{1c}) + (1-g_1) \exp(-t/\tau_{2c})$, where τ_{1c} and τ_{2c} are the shorter and longer rotational correlation times, respectively, and g_1 is the fractional amplitude corresponding to τ_{1c}. In practice, g_1 represents the fraction of unbound (more rapidly rotating) fluorophore, and $(1-g_1)$ represents the fraction of bound (more slowly rotating) fluorophore. The BCECF rotational diffusion coefficient in a given sample relative to that in water, $(D/D_0)_{rot}$, was determined from the ratio of τ_1 measured in buffer to that measured in the sample (Fushimi and Verkman, 1991).

Binding and stopped-flow polarization measurements

Both the extent and the kinetics of probe binding to intracellular structures will enter into the theoretical model developed in the next section. The methodology used to characterize these quantities was as follows.

The extent of BCECF binding to cytoplasmic components was determined by picosecond anisotropy measurements, as described above, and by confocal microscopy. For the latter measurements, a monolayer of 3T3 fibroblasts was permeabilized with 40 μg/ml digitonin for 30 min at 5° C and equilibrated with 100 μM BCECF acid in PBS for 15 min. BCECF fluorescence in cell cytoplasm and the adjacent solution was measured by confocal microscopy (Technical Instruments, San Francisco, CA; 100X objective, 0.6 μm measured z-axis resolution). Binding was determined from the ratio of intracellular to extracellular fluorescence, corrected for the non-aqueous cell volume of ~20 %.

The kinetics of BCECF binding in a 10 % suspension of fibroblast cytoplasm and in a 5 % albumin solution was determined by stopped-flow fluorescence polarization using a Hi-Tech SF51 apparatus. The method exploits the fact that steady-state fluorescence polarization (or anisotropy) increases as probe binds. Equal volumes of a 100 μM BCECF solution and a cytoplasm or albumin solution were mixed in < 1 ms in a stopped-flow

apparatus. The time course of fluorescence (480 nm excitation, > 515 nm emission) was measured at a rate of 0.1 ms/point. To determine the time course of steady-state fluorescence anisotropy, the incident light was vertically polarized and the emitted fluorescence was measured through vertically and horizontally oriented analyzing polarizers.

2.4 Results

2.4.1 Theory for Slowed Diffusion in Cytoplasm

The purpose of this mathematical section is to provide a framework for the analysis of translational diffusion data in cell cytoplasm. It is assumed that cell cytoplasm consists of an aqueous fluid-phase compartment bathing a matrix of mobile and immobile particles that are much larger than the water molecules and small solutes. It is further assumed that three independent factors act to decrease the diffusion coefficient of a small solute in cytoplasm (D) relative to that in water (D_0),

$$D/D_0 = F_1(\eta) \cdot F_2(D_u, \{D_{b,i}, f_{b,i}\}) \cdot F_3(\{n_i, V_i\}) \qquad (2\text{-}1)$$

where F_1, F_2, and F_3 are defined below.

The function $F_1(\eta)$ describes the slowing of net solute translation due to an increase in true fluid-phase cytoplasmic viscosity. Such an increase would reflect some solute-induced perturbation in solvent structure, which need not be specified. The functional form for F_1 follows from the reciprocal relationship between the diffusion coefficient and the viscosity, and can be written

$$F_1(\eta) = \eta_0/\eta \qquad (2\text{-}2)$$

where η_0 is the viscosity of water, and η is the true fluid-phase microviscosity of cytoplasm. The fluid-phase viscosity η can be obtained from measurements of solute rotational dynamics, or potentially of short-range solute translational dynamics. The fluid-phase viscosity cannot be obtained from measurements of macroscopic cytoplasmic viscosity; indeed, the macroscopic viscosity can be many times greater than the fluid-phase viscosity (Furukawa et al., 1991; Scalettar and Abney, 1991). Eq. (2-2) predicts that if the fluid-phase viscosity increased by a factor of 2, D/D_0 would decrease by a factor of 2.

The function $F_2\,(D_u,\{D_{b,i},f_{b,i}\})$ describes the net slowing of solute translation due to transient binding of solute molecules to cytoplasmic structures. For the simplest case in which there is solute binding only to one macromolecular species, the measured FRAP diffusion coefficient has been shown to be a linear combination of the diffusion coefficients for the bound and unbound solute, weighted by the appropriate mole fractions (Elson and Qian, 1989; Elson and Reidler, 1979; Jähnig, 1981; Koppel, 1981). This expression can be generalized to describe multiple bound species; the form for F_2 is taken as the ratio of the weighted diffusion coefficient of the bound and unbound solute to the diffusion coefficient of the unbound solute. If D_u is the diffusion coefficient of unbound solute, $D_{b,i}$ the diffusion coefficient of the *ith* bound solute, and $f_{b,i}$ the fraction of total solute bound to component i, then

$$F_2\,(D_u,\{D_{b,i},f_{b,i}\}) = f_u + \Sigma\,(D_{b,i}/D_u)\,f_{b,i} \qquad (2\text{-}3a)$$

where

$$f_u + \sum_i f_u = 1 \qquad (2\text{-}3b)$$

It is assumed in Eq. (2-3) that the kinetics of solute binding and unbinding is fast compared to the characteristic time for translational diffusion in a FRAP experiment. In the FRAP

studies described below, Eq. (2-3) applies for submillisecond binding kinetics. For a simple situation in which 50 % of the solute is unbound and 50 % is bound at any instant to immobile intracellular structures ($f_u = 0.5$, $\{D_{b,i}\} = 0$), Eq. (2-3) predicts that D/D_0 would decrease by a factor of 2.

The function F_3 ($\{n_i,V_i\}$) describes the slowing of solute translation due to collisional interactions with cytoplasmic structures, where in general there are n_i structures of type i, each having volume V_i. Two theories have been used to describe the effects of "volume occlusion" by mobile obstacles on diffusion: a stretched-exponential (SE) model (Furukawa et al., 1991; Phillies, 1989) and a free-volume (FV) model (Fujita, 1961; Furukawa et al., 1991; Landry et al., 1988). The SE model has been used to describe the diffusion of relatively large, Brownian particles, whereas the FV model has been used to describe solvent diffusion. Because BCECF is a small (nearly solvent-sized) solute, its motion can be satisfactorily described by both models. Both are applied models to demonstrate model-independence of the results.

The stretched-exponential model was initially developed to give a good an empirical fit to diffusion data in crowded media. Recently, it has been shown that an SE equation can be derived theoretically. The SE model has been found to fit diffusion data well over a wide range of solute and occluding molecule sizes (Phillies, 1989), and has been elegantly used to describe the diffusion of large solutes in cell cytoplasm (Hou et al., 1990). For a single class of obstacle, the SE model predicts

$$F_{3,SE}(n_i,V_i) = \exp\left[-\alpha\,(n_i\,V_i)^{\nu}\right] \tag{2-4}$$

where n_iV_i is the volume fraction occupied by the occluding molecule, and the prefactor α and the exponent ν are scaling parameters. The values of α and ν can be determined empirically by fitting (2-4) to data, and they can be calculated independently from theory. For small solutes, ν is usually found to be near unity (Furukawa et al., 1991), while α

depends on the concentration units.

In contrast, the free-volume model was derived from a molecular description of diffusion. The FV model is based on the assumption that solute diffusion in crowded media is rate-limited by the availability of "free-volume", i.e., volume sufficiently devoid of obstacles that it can be occupied by solute. The diffusion coefficient is assumed to follow an Arrhenius equation in which the (model-dependent) activation energy reflects the probability of finding appropriate free-volumes. A successful and simple formulation of the FV model was derived by Fujita (1961). For a single class of obstacle, the FV model predicts

$$F_{3,FV}(\varphi) = \exp\left[\frac{-B_d\,\beta(T)\,(\varphi_0 - \varphi)}{\left[f(0,T) + \beta(T)\varphi_0\right]\left[f(0,T) + \beta(T)\varphi\right]}\right] \qquad (2\text{-}5)$$

where φ is the free-volume fraction of solvent, φ_0 is φ in the absence of obstacles, f(0,T) is the temperature-dependent free-volume in the absence of solvent, $\beta(T)$ describes the free-volume difference between solvent and obstacles (in the appropriate reference states), and B_d describes the minimum free volume required for solute displacement. f(0,T) and $\beta(T)$ generally have small, positive values, and B_d and φ_0 are taken to be unity. Although they have physical significance, FV parameters are usually determined by parameter regression, rather than independent experiment.

2.4.2 Validation of diffusion coefficient measurement by FRAP

The quantitative determination of BCECF diffusion coefficients in the aqueous phase of cell cytoplasm was based on the comparison of photobleaching recovery curves in cells with those in calibration solutions. Consistency in cell data therefore hinges critically on consistency in calibration data. Fig. 2.2 A shows original recovery curves for

Figure 2.2. Validation of diffusion coefficient measurement. A. Photobleaching recovery curves for solutions consisting of 240 μM BCECF in PBS containing 0-49% (w/w) sucrose to give viscosities of 1.02 (a), 4.5 (b), 9.1 (c), and 13.3 (d) cP. Sample thickness was 5 μm. The beginning of the photobleaching pulse is indicated by the arrow; at this time a shutter in the emission path was closed. The smooth curves through the data were obtained by biexponential regression. The dashed horizontal line denotes the value of $F(\infty)$. **B.** Dependence of recovery half-times ($\tau_{1/2}$) on solution viscosity (η). Data from a series of calibration solutions (mean ± SEM, n=4) are shown with a fitted line. **C.** Photobleaching recovery curves for the 4.5 cP calibration solution and normal cells (23° C, isosmotic volume), demonstrating that both follow the same biexponential time course. The cell data were overlaid onto the calibration data by rescaling the associated ordinate and abscissa, while leaving the exponential amplitudes and time constants (which determine curve shape) unchanged.

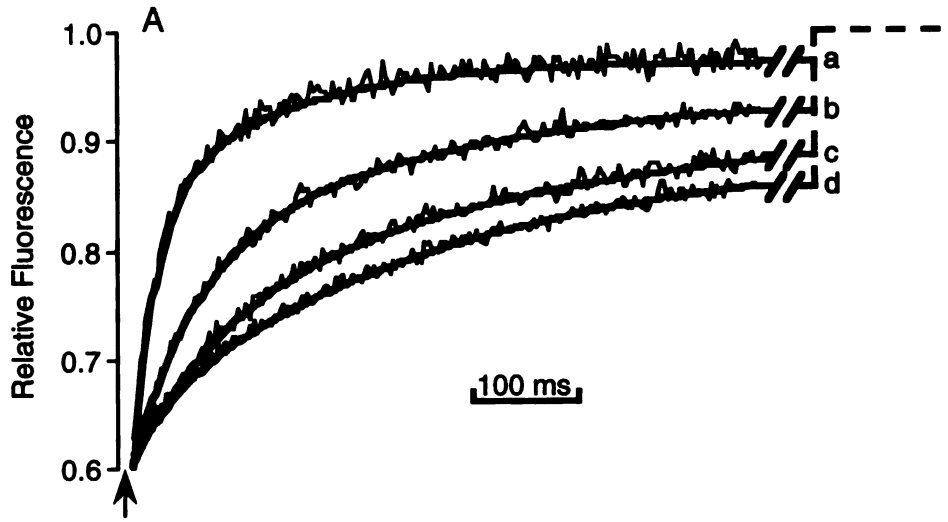
A
1.0
0.9
0.8
0.7
0.6
Relative Fluorescence
a
b
c
d
100 ms

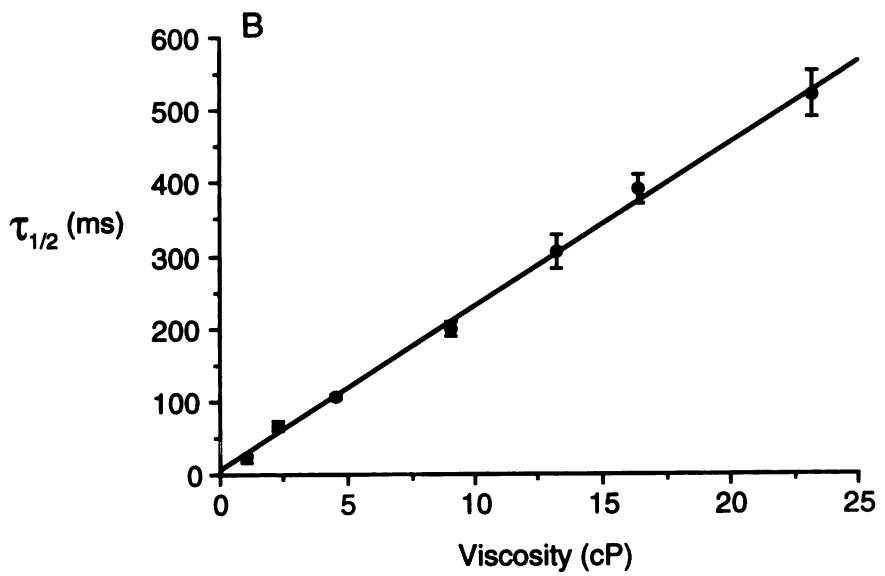
B
600
500
400
300
200
100
0
$\tau_{1/2}$ (ms)
0
5
10
15
20
25
Viscosity (cP)

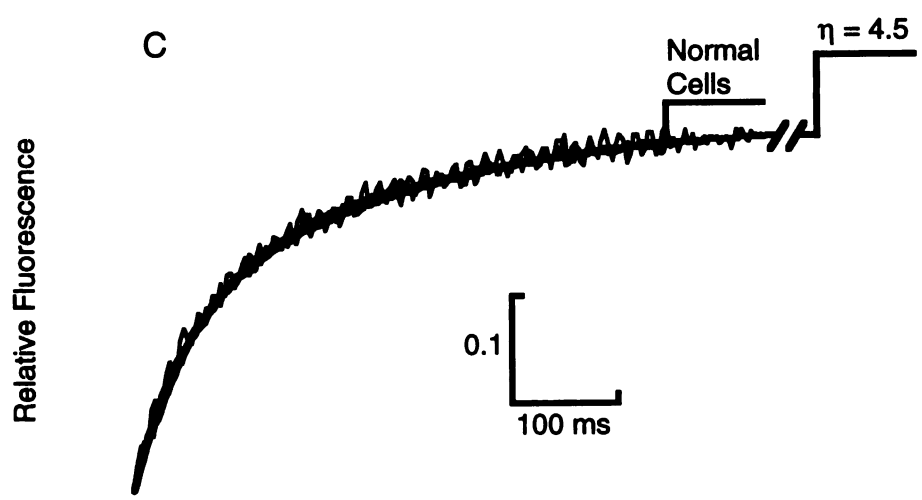
C
Normal
Cells
η = 4.5
Relative Fluorescence
0.1
100 ms

calibration solutions consisting of BCECF and various sucrose concentrations in PBS, giving viscosities between 1.02 and 13.3 cP. The intensity of the photobleaching beam was set to maintain the percent photobleaching in the range 25 - 45 %. The fluorescence at long times after photobleaching, $F(\infty)$, was nearly equal to that prior to photobleaching, F(-), indicating that all of the BCECF was mobile. In a total of 188 FRAP measurements made on calibration solutions, the percent recovery was 98 ± 1 % (SEM). As solution viscosity increased, the rate of recovery decreased.

The half-time ($\tau_{1/2}$) for recovery provided a quantitative measure of the recovery rate. Because a rigorous theoretical description of the recovery-curve shape would be very complicated and has not yet appeared in the literature (see Discussion), a functional form for the recovery curve shape was chosen empirically. Although a monoexponential function did not fit the data well, a biexponential function fit the data very well as shown by the fitted curves in Fig. 2.2 A. Plots of residuals showed no systematic deviation of experimental data from the biexponential fit. In addition, the shape of the biexponential curve was nearly the same in all experiments as indicated by the similar ratios of exponential time constants. The invariance of recovery curve shape provides direct justification for the use of $\tau_{1/2}$ as a single parameter measure of recovery rate. Fig. 2.2 B shows a linear relationship between $\tau_{1/2}$ and viscosity for a set of calibration solutions. Although the slope of this calibration plot varied from day to day because of slight variations in beam profile and alignment (slope 21 ± 4.2 ms/cP, SD, n=6), the slope generally changed by < 20 % from the beginning to the end of a 6 h set of measurements.

Since Gaussian beams diverge with distance from the focal plane, diffusion coefficients can, in principle, depend on cell thickness. However, for the 16X objective used here, the Rayleigh range (i.e., half the distance over which the beam radius remains within ~ 40 % of its minimum value) is quite large, ~ 50 μm. Not surprisingly, measured $\tau_{1/2}$'s did not increase as the objective focal point was positioned up to 10 μm above or below the center of a thin (5 μm) calibration sample, or as sample thickness was increased from 2 to

50 μm. Since the maximum thickness of the 3T3 fibroblasts is < 2 μm, incident beam divergence is not important in our experiments. The possible dependence of diffusion coefficient on beam spot size is considered in the Discussion.

Taken together, the findings above establish a rigorous basis for the interpretation of photobleaching curves obtained in cell cytoplasm.

2.4.3 FRAP experiments in cells

Photobleaching experiments were conducted using a 3-μm beam spot, which covers < 1 % of the area of a Swiss 3T3 fibroblast (Luby-Phelps et al., 1987). The beam was positioned to photobleach cytoplasm in an area not directly adjacent to the nucleus or cell edge. No more than one photobleaching experiment was performed on a single fibroblast. Cell experiments were calibrated using 5 μm thick standard solutions; the validity of this approach is demonstrated in Fig. 2.2 C, in which it is shown that recovery curves follow identical biexponential time courses in calibration solutions and cells. Figs. 2.3 and 2.4 show original recovery curves obtained from fibroblasts under a variety of conditions. For a fixed bleaching intensity, the percent bleaching increased with decreasing cell volume and increasing glycerol concentration. However, the associated recovery times are independent of percent bleaching for the relatively shallow bleaching depths employed, as determined in separate experiments on calibration solutions and cells. Effective cytoplasmic viscosities derived from a series of measurements are summarized in Figs. 2.5 and 2.6 A (see below). The vast majority of BCECF was mobile in cell cytoplasm as shown by percent recoveries of > 90 %. In cells bathed in PBS at 23° C, the ratio of the BCECF diffusion coefficient in cytoplasm to that in water (D/D_0) was 0.27 ± 0.01 (SEM, n=24). The distribution of D/D_0 values was unimodal without any systematic dependence on the time between BCECF loading and measurement, cell passage number, or cell density. D/D_0 was strongly influenced by changes in cell volume (Figs. 2.3 and 2.6 A) or

Figure 2.3. Effects of changes in cell volume on fluorescence photobleaching recovery curves for BCECF-labeled Swiss 3T3 fibroblasts. Cell volume was adjusted after BCECF labeling by incubating cells in media of various osmolarities. Hypoosmotic media were made by addition of sucrose to PBS; hyperosmotic media were made by dilution of PBS. Recovery curves are shown for control cells (23° C, isosmotic volume), and cells at 0.33, 0.5, and 2 times isosmotic volume.

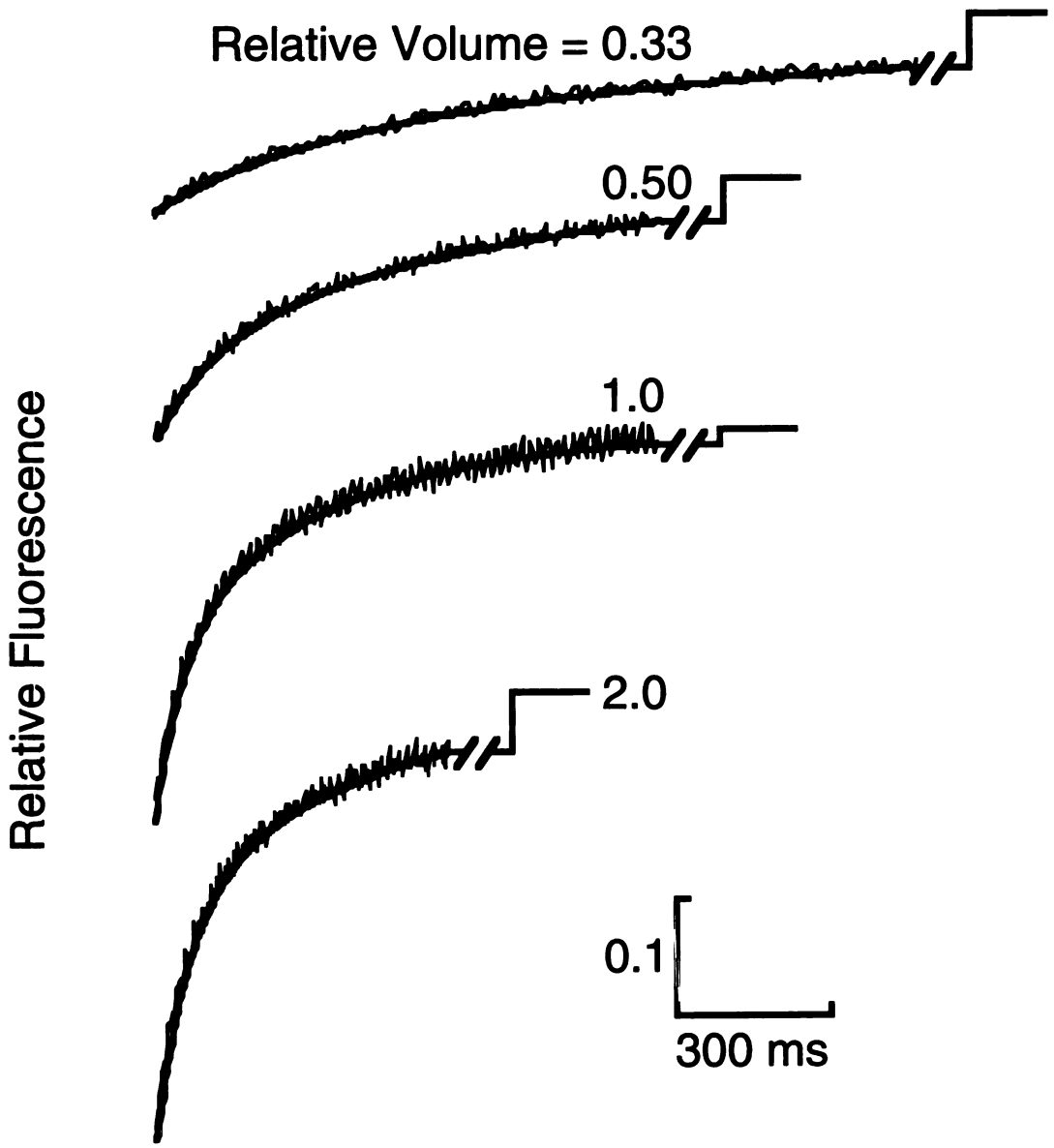
Relative Volume = 0.33
0.50
1.0
2.0
Relative Fluorescence
0.1
300 ms

Figure 2.4. Effects of changes in aqueous-phase viscosity on fluorescence photobleaching recovery curves for BCECF-labeled Swiss 3T3 fibroblasts. Aqueous-phase viscosity was adjusted following BCECF labeling by incubating cells in media containing various concentrations of glycerol for 15 min at 23° C. Media were made by addition of glycerol to PBS; ionic strength was maintained at 300 μM by addition of NaCl. Recovery curves are shown for control cells (23° C, 0 % glycerol), and cells in 28 and 48 % (w/w) glycerol.

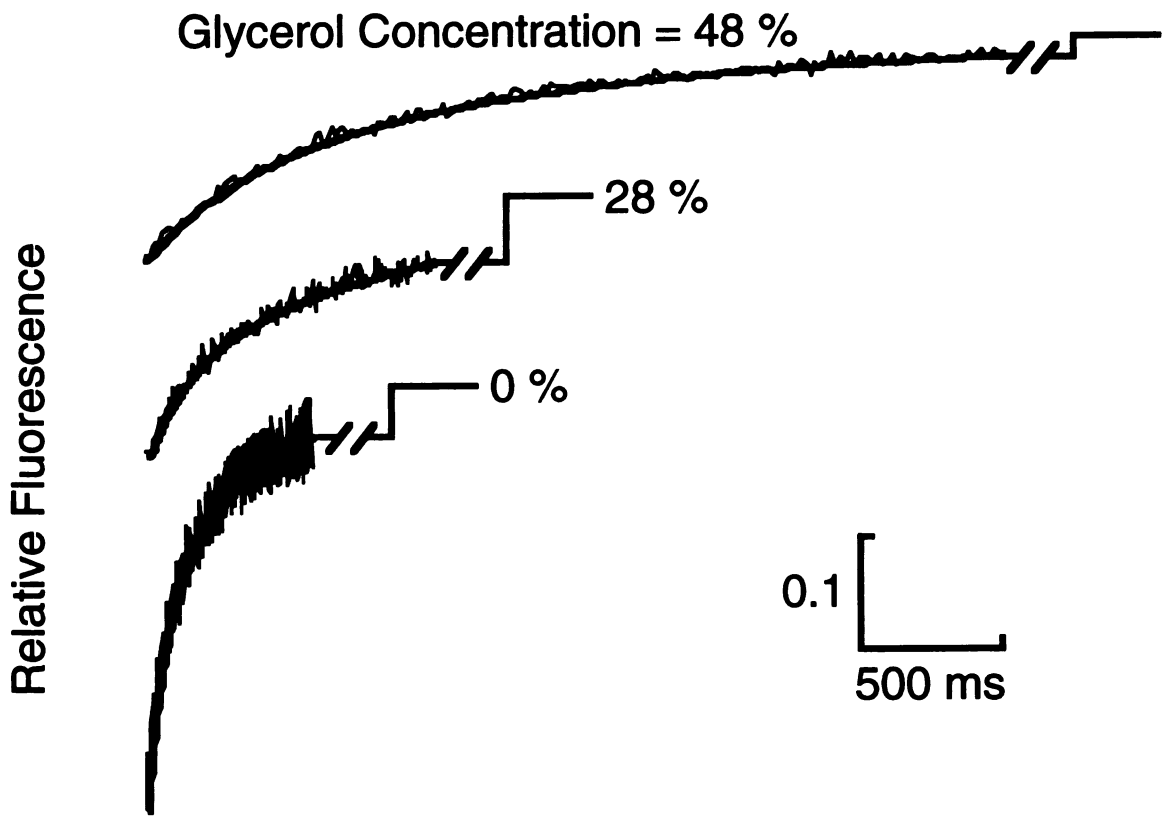
Glycerol Concentration = 48 %
28 %
0 %
Relative Fluorescence
0.1
500 ms

Figure 2.5. Slowing of BCECF translation in fibroblasts bathed in buffers containing glycerol. BCECF translational diffusion was measured by FRAP. The ordinate (mean ± SEM) is the ratio of the BCECF diffusion coefficient in control cells (- glycerol) to that in cells bathed in 28 or 48 % glycerol (+ glycerol). The abscissa is the viscosity (relative to water) corresponding to each glycerol concentration. Data are mean ± SEM for 13 - 17 measurements.

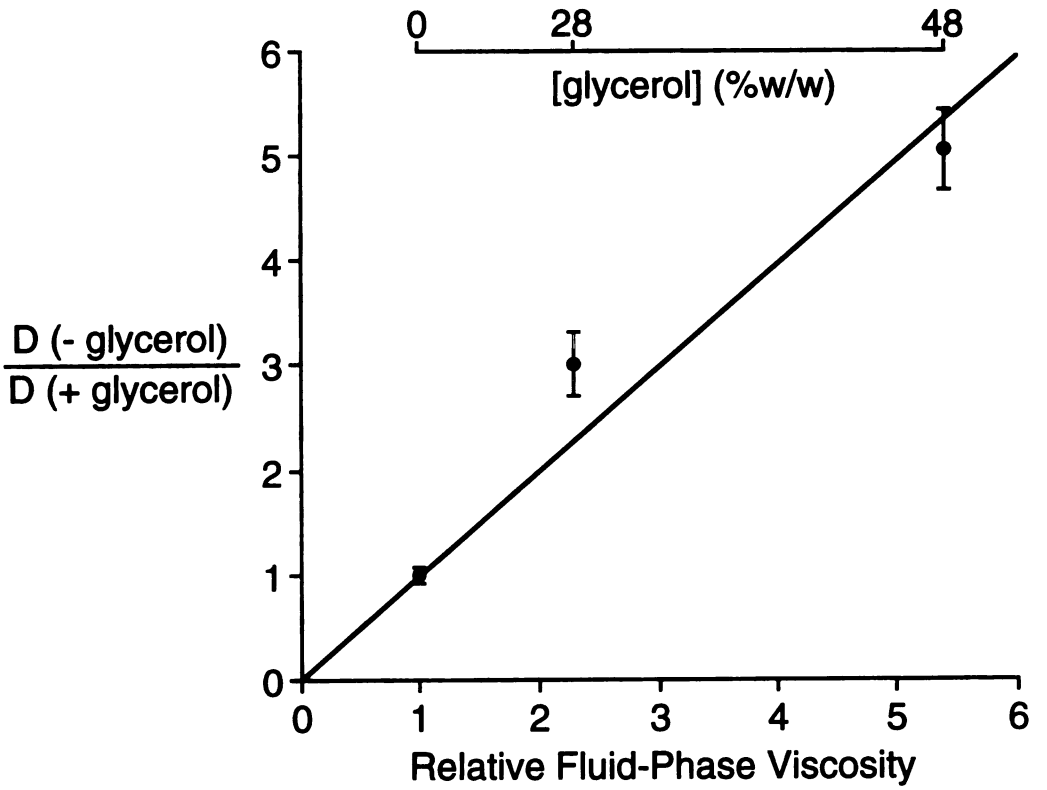
0
28
48
[glycerol] (%w/w)
D (- glycerol)
D (+ glycerol)
6
5
4
3
2
1
0
0
1
2
3
4
5
6
Relative Fluid-Phase Viscosity

Figure 2.6. Slowing of BCECF translation due to volume occlusion. A. D_0/D for BCECF-loaded 3T3 fibroblasts measured as a function of relative cell volume. Data are mean ± SEM for 3 - 7 measurements. The cell data were fitted to the SE and FV models by a least-squares procedure that fixed the parameters derived in (B) and floated as a fitting parameter the factor that converts inverse cell volume to dextran concentration. The value of this conversion factor corresponding to an ordinate value of 1 in (A) gives the "effective percentage dextran" associated with isosmotic conditions. The derived effective dextran concentration is 13 %; substituting this value into the SE and FV models gives F_3 = 0.40. The solid line indicates the fit to the cell data obtained by this procedure; the dashed lines indicate the values associated with a 15 % error in the calculated value for the effective percentage dextran. The measured values all lie well within the 15 % error envelope, and we thus estimate the error in the calculated value of F_3 to be ~ 10 %. **B.** D_0/D for 100 μM BCECF in PBS solutions containing the indicated percentages (w/w) of dextrans of MW 10 kD (○), 39 kD (●), 66 kD (Δ), 82 (▲) and 2000 kD (■). Additional values of D_0/D are given for agarose gels (❑) and PBS alone (×; no dextran or agarose). Data were fitted to the SE and FV models; fitted parameters were: $\alpha = 0.058$ and $\nu = 1.06$ [SE model, Eq. (2-4)] and $B_d = 1$, $f(0,T) = 0.0034$, and $\beta(T) = 0.015$ [FV model, Eq. (2-5)]. Errors in fitted parameters probably range from 5 to 15 % (Furukawa et al., 1991). The curve is the fit to the SE model; the fit to the FV model is virtually superimposable (not shown).

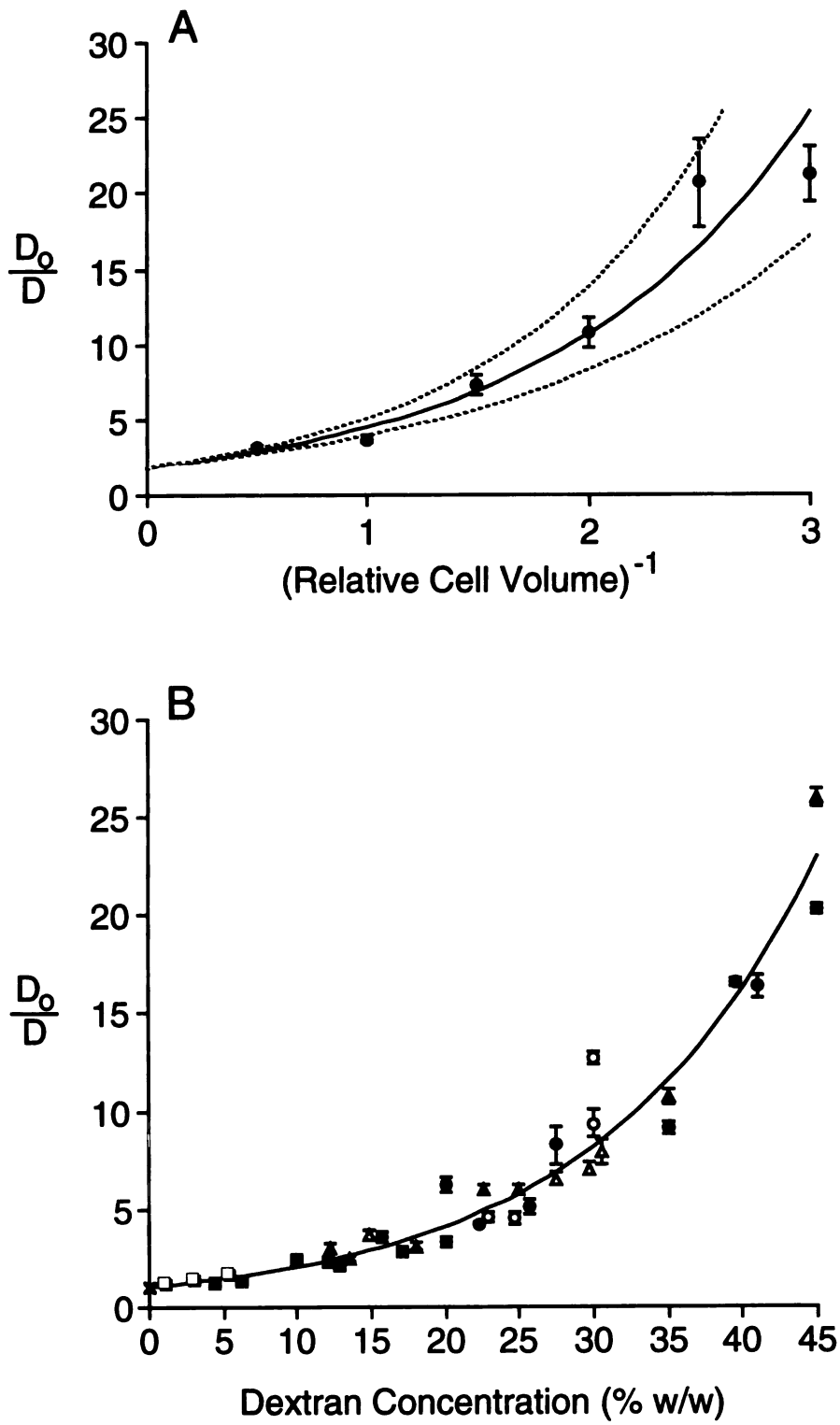
A
30
25
20
15
10
5
0
$\frac{D_o}{D}$
0
1
2
3
(Relative Cell Volume)$^{-1}$
B
30
25
20
15
10
5
0
$\frac{D_o}{D}$
0
5
10
15
20
25
30
35
40
45
Dextran Concentration (% w/w)

addition of glycerol to the bathing medium (Figs. 2.4 and 2.5). In the following sections, the results of these experiments and others will be used to characterize systematically the factors that slow BCECF diffusion in cytoplasm based on the theoretical considerations described in the previous section.

Slowed BCECF diffusion in cytoplasm: I. Fluid-phase viscosity

The measurement of time-resolved anisotropy provides independent information about the rotation of bound and unbound fluorophore. Moreover, because the rotation of small solutes is not hindered by collisional interactions with intracellular structures when the spacing between structures is much larger than the solute diameter (Drake and Klafter, 1990), the fluid-phase viscosity can be estimated from the rotational diffusion coefficient of the unbound BCECF. Time-resolved anisotropy was measured in BCECF-labeled fibroblasts under the conditions used for FRAP measurements as described in Methods. In 4 sets of control cells bathed in isosmotic buffer, BCECF rotational correlation times, τ_{1c} and τ_{2c}, were 290 ± 12 ps and 12 ± 3 ns, respectively; the fraction of (bound) BCECF with the longer correlation time was 0.19 ± 0.02. In PBS, a single rotational correlation time of 226 ps was measured. These results are in agreement with previous measurements made under similar conditions (Fushimi and Verkman, 1991). At isosmotic cell volume, the relative diffusion coefficients for BCECF rotation and translation were 0.78 ± 0.03 and 0.27 ± 0.01. As cell volume increased from 0.33 to 2 times isomotic volume, the relative rotational diffusion coefficient remained nearly constant (0.76-0.79), while the relative translational diffusion coefficient increased from 0.047 to 0.32 (Figs. 2.3 and 2.6 A). Thus rotation in the cytoplasm is less hindered and less sensitive to changes in cell volume than is translation.

To confirm the sensitivity of BCECF rotation to fluid-phase cytoplasmic viscosity and to test the assumption that F_1 is independent of F_2 and F_3 (see Theory section), BCECF translation and rotation were measured in cells equilibrated with 28 and 48 %

glycerol. These glycerol concentrations increase the macroscopic viscosity of aqueous buffers by 2.3- and 5.4-fold (Weast, 1986). As predicted, the BCECF rotational diffusion coefficient (obtained from τ_{1c} measurements) decreased by approximately 2- and 5-fold, confirming the sensitivity of the anisotropy decay measurement. Figs. 2.4 and 2.5 show the effect of glycerol addition on the BCECF translational diffusion coefficient. The slope (0.98) of the best-fit line through the data in Fig. 2.5 demonstrates that the BCECF translational diffusion coefficient is nearly halved for each doubling of fluid-phase viscosity. The parallel increase in fluid-phase viscosity and BCECF translational recovery time provides direct support for the assumption that F_1 is independent of F_2 and F_3.

In summary, our data indicate that fluid-phase cytoplasmic viscosity differs to a small but significant extent from the viscosity of water. Inserting the viscosity data into Eq. (2-2) gives $F_1 \sim 0.78 \pm 0.03$.

Slowed BCECF diffusion in cytoplasm: II. Binding

The slowing of BCECF diffusion due to binding depends on the fraction of bound BCECF in cytoplasm, the mobility of bound BCECF, and the kinetics of binding. The fraction of bound BCECF was measured by two methods. First, the fractional anisotropy loss due to rapid BCECF rotation, 0.81 ± 0.01, provides a direct measure of the fraction of BCECF that rotates freely. These data suggest that 19 % BCECF is bound, assuming that there is no rapidly rotating "weakly bound" BCECF (see Discussion). As cell volume changes from 0.33 to 2 times isosmotic volume, there is little change in the percentage of bound BCECF (range 18-21 %). Second, the fraction of bound BCECF was estimated by Nipkow wheel confocal microscopy in digitonin-permeabilized cells that were equilibrated with 100 μM BCECF (acid, not acetoxymethylester form). BCECF intensity was measured in cells and in 2 μm thick films of the BCECF solution used for equilibration. In 4 experiments, the ratio of intracellular to extracellular BCECF (corrected for cell aqueous volume) was 1.02, indicating that ~ 20 % of intracellular BCECF is bound.

The translational mobility of bound BCECF was estimated by assuming that dye binds to cellular protein and thus diffuses like cellular protein. In previous FRAP studies (Jacobson and Wojcieszyn, 1984; Kreis et al., 1982), the cytoplasmic diffusion coefficients of native and exogenous proteins ranging in size from 12 to 440 kD were found to be 50-1000-fold smaller than that measured here for BCECF. This result, plus the fact that some dye probably binds to truly immobile structures, suggests that the ratio D_b/D_u is very close to zero.

An attempt was made to estimate the mobility of bound fluorophore by reacting intracellular proteins non-selectively with carboxyfluorescein succinimidyl ester. Cells were hypotonically loaded with 500 μM carboxyfluorescein succinimidyl ester for 15 min and then incubated at 37° C in PBS for 60 min. FRAP data obtained from the labeled cells showed small percent bleaching relative to data obtained for aqueous or intracellular BCECF; the fluorescence recovery had a complex multi-exponential time course. The results were difficult to interpret because: (a) free dye apparently was considerably more bleachable than bound dye, and thus the recovery curve was dominated by the diffusion of unbound dye molecules, and (b) the intracellular distribution of the covalently bound dye, as determined by fluorescence microscopy, was quite different from that of the non-covalently bound BCECF.

The kinetics of BCECF binding to intracellular components was estimated by stopped-flow fluorescence polarization as described in Materials and Methods. BCECF binding to a 10 % cytoplasmic homogenate and to a 5 % albumin solution gave a measurable increase in polarization. 85-90 % of the increased polarization occurred within the instrument dead time of 1.5 ms; ~ 80% of the remaining increase in polarization had a half-time of 3-5 ms. These data confirm that the binding and unbinding of BCECF occurs on a time scale much faster than the half-times for photobleaching recovery.

In summary, the submillisecond BCECF binding kinetics justifies the use of Eq. (2-3) to describe binding effects. Taken together with the very low mobility of bound dye,

Eq. (2-3) gives $F_2 \sim 0.81 \pm 0.01$.

Slowed BCECF diffusion in cytoplasm: III. Collisional interactions

The dependence of D/D_0 on cell volume provides information that can be used to evaluate the effects of collisional interactions on BCECF translational diffusion. Because BCECF rotational diffusion and binding are influenced little by changes in cell volume as shown above, the large effects of cell volume on translational diffusion are due mainly to changes in the fraction of intracellular volume occupied by the cytomatrix.

The effects of "volume occlusion" by mobile obstacles were investigated empirically by measurement of BCECF diffusion in PBS solutions containing dextrans of different size and composition. Separate studies of anisotropy decay and binding showed little binding of BCECF to dextran and little change in aqueous-phase viscosity with increasing dextran concentration. Fig. 2.6 B shows that D_0/D increases non-linearly as the solution volume occupied by dextran increases. The dependence of D_0/D on percentage dextran was independent of dextran size in the range 10-2000 kD, in general agreement with results in the literature on the diffusion of small solutes in solutions containing much larger occluding solutes (Blum et al., 1986; Furukawa et al., 1991). The data fitted well to both the stretched-exponential and free-volume models as described in Theory.

The effects of "volume occlusion" by immobile obstacles were also investigated empirically. FRAP experiments were performed in 50 μm thick films of 1, 3 and 5 % low-gelling-temperature agarose gels containing 500 μM BCECF in PBS. The D_0/D values given in Fig. 2.6 B (filled circles) were in agreement with the results for equivalent dextran percentages. Unfortunately, gels with agarose concentrations greater than 5 % are difficult to prepare and were not studied. However, the fact that BCECF diffusion is not sensitive to dextran size (and hence dextran mobility) suggests that obstacle mobility is much less important than obstacle concentration in determining D/D_0, at least for obstacles with sizes > 10 kD. Hence, the dextran data probably provide an adequate model for the effects of

volume occlusion on BCECF translation.

Fig. 2.6 A shows the relationship between D_0/D for BCECF translation and the reciprocal cell volume, which is assumed to be proportional to the concentration of the cytomatrix. The data were fitted to the stretched-exponential and free-volume models using parameters from Fig. 2.6 B and taking the percentage occluded volume (under isosmotic conditions) as a floating parameter. The data were fitted well when 13 % of isosmotic cell volume is effectively occupied by occluding molecules. Because the majority of occluding molecules in cell cytoplasm are predicted to be in the 10-2000 kD size range, the dextran solutions provide a reasonable model for cell cytoplasm. From the data in Fig. 2.6 B, 13 % dextran gives an F_3 value of 0.40 ± 0.04.

Composite effects of F_1, F_2 and F_3

The product of F_1, F_2 and F_3 determined independently above is 0.25 ± 0.03. This value is in good agreement with the D/D_0 of 0.27 ± 0.01 measured for BCECF translational diffusion in cell cytoplasm.

Additional cell experiments with a smaller photobleaching spot size

Some cell experiments were performed using a 100X objective (Nikon, numerical aperture 1.3) with a 0.4 μm beam radius. First, there was significant dye rearrangement during the 2-3 msec bleaching time, making the effective bleached area much larger than the beam radius. However, the use of standard solutions obviated the need for precisely characterizing the bleached area. Second, the bleach and probe beams generated by the 100X objective diverge substantially. However, we found that $\tau_{1/2}$ did not increase as the objective focal point was positioned up to 2 μm above or below the center of a thin (5 μm) calibration sample, or as sample thickness was increased from 0 to 5 μm. Beam divergence therefore did not affect our experiments on the < 2 μm thick 3T3 fibroblasts. For these experiments, the standard curves were again linear, but the recovery times were

significantly smaller (slope of calibration plot as in Fig. 2.2 B = 3.5 ± 0.7 ms/cP, SD, n=6). Experiments on control cells yielded D/D_0 = 0.24 ± 0.01 (SEM, n=55, 23° C) at isomotic volume. The glycerol experiments (as in Fig. 2.5) gave D(-glycerol)/D(+glycerol) of 1.0 , 2.1, and 5.3 for cells incubated in 0, 28, and 48 % glycerol. The cell volume experiments (as in Fig. 2.6 A) gave D_0/D of 3.0, 4.2, 13, and 23 for cell volumes of 2, 1, 0.5, and 0.33 times isosmotic volume. The latter experiments imply that F_3 = 0.56, corresponding to an equivalent dextran concentration of 13 %. The product of F_1, F_2, and F_3 is 0.28 ± 0.03, in good agreement with the value of 0.24 ± 0.01 obtained with the 100X objective.

2.5 Discussion

The goals of this study were to measure the translational mobility of a small solute in cell cytoplasm and to construct a consistent physical model of the factors that hinder solute translation. A small solute, rather than a labeled dextran or ficoll, was chosen as the probe molecule so that the results would apply to small intracellular metabolites without the need to extrapolate data obtained for large probes to zero probe molecular size. The translational motion of a small solute in cell cytoplasm has not been quantified previously by photobleaching recovery techniques; because of the very fast recovery times, only a lower limit has been established for the translational diffusion coefficient of fluorescein-type probes (Jacobson and Wojcieszyn, 1984). We found that the fluorescent probe BCECF was mobile in cell cytoplasm and had short photobleaching-recovery times that yielded a translational diffusion coefficient relative to that in water (D/D_0) of 0.27 ± 0.01. This value is significantly less than unity and less than the BCECF rotational diffusion coefficient relative to that in water $(D/D_0)_{rot}$ of 0.78 ± 0.03. Theoretical analysis and experiments on model solutions and cells were carried out to explain these results and to reconcile the differences. It was concluded that the low D/D_0 for BCECF translation could

be quantitatively attributed to the combination of 3 independent factors: increased fluid-phase cytoplasmic viscosity, intracellular BCECF binding, and BCECF collisional interactions with cytoplasmic structures. Moreover, the disparity between the relative translational and rotational diffusion coefficients was found to arise because rotation is relatively insensitive to the factor that most significantly perturbs translation: collisions with occluding macromolecules. The value for D/D_0 and its physical basis have important implications for cellular processes as discussed below.

The quantitative analysis of the photobleaching recovery of a cytoplasmic probe required special technical considerations. A rigorous theory exists for the calculation of recovery-curve shape for the 2-dimensional diffusion of a fluorophore in a spot photobleaching experiment (Axelrod et al, 1976). The theory assumes a Gaussian beam profile, perfect alignment of bleach and probe beams, no movement of unbleached dye into the bleached area during the bleaching pulse, first-order bleaching kinetics, and accurate knowledge of beam diameter. A similar theory describing the 3-dimensional diffusion of fluorophore in a region illuminated by a diverging Gaussian beam does not exist. Furthermore, studies of 2-dimensional systems have shown that results extracted from theory can be greatly affected by difficulties inherent in obtaining reproducible beam profiles and alignment (Barisas, 1980), bleach pulses that are short relative to the recovery kinetics (Bertch and Koppel, 1988), and purely first-order bleaching kinetics (Bjarneson and Petersen, 1991). For these reasons, our approach was to compare recovery curves for cells with curves obtained for a series of thin films of aqueous buffers having known viscosity. Recovery curves were obtained in the calibration solutions before and after every set of experiments to ensure stability of beam profile and alignment, and to provide a calibration relation for determination of apparent viscosity from recovery half-times. The use of calibration standards makes unnecessary the characterization of beam profile and alignment because the standard and samples are bleached and probed under identical conditions. Another important design criterion was the use of a very brief bleach pulse to

minimize diffusion of unbleached dye into the bleached area during the bleaching pulse. In these experiments, a 2-3 ms bleach pulse with 5000:1 attenuation ratio for bleach-to-probe beam intensity was generally used.

Photobleaching experiments monitor diffusion over micron-scale distances. The distance probed is approximately proportional to $(\tau_{1/2})^{1/2}$, and thus the distance scale probed here with the 16X objective (3 μm) is probably about twice that probed with the 100X objective. (The characteristic distance scale monitored by the 100X objective is significantly larger than its spot size because dye moves extensively during the bleaching pulse for this objective.) The consistency between the diffusion coefficients obtained with the 16X ($D/D_0 = 0.27 \pm 0.03$) and 100X ($D/D_0 = 0.24 \pm 0.03$) objectives suggests that diffusion within the cytoplasm is not sensitive to distance on the micron distance scale. This observation is in accord with theoretical predictions that the diffusion coefficient should be sensitive to distance only in a regime that is comparable to the obstacle spacing (Pusey and Tough, 1985; Scalettar and Abney, 1991). The distance scale studied here is typical of that studied in spot photobleaching experiments of cytoplasmic diffusion (1.5 - 6.0 μm; Jacobson and Wojcieszyn, 1984; Kreis et al., 1982; Luby-Phelps and Taylor, 1988; Luby-Phelps et al., 1986, 1987, 1988; Wojcieszyn et al., 1981) and smaller than that studied in pattern photobleaching experiments (11.8 μm to one-half cell size; Blatter and Wier, 1990; Wang et al., 1982).

The rotational motion of small fluorophores was described by an anisotropy decay model containing two rotational correlation times that differed by a factor of > 20. From studies of aqueous buffers containing glycerol to increase viscosity and proteins to bind fluorophore (Fushimi and Verkman, 1991), the shorter correlation time was assigned to rotation of unbound dye and the longer correlation time to rotation of bound dye. The agreement between estimates of intracellular BCECF binding by anisotropy decay and intracellular partitioning (measured by confocal microscopy) supports the assignment of the shorter correlation time to the rotation of unbound dye. However, there are several caveats

in the interpretation of anisotropy data that deserve mention. Although the two-component anisotropy decay model provided a good statistical fit to phase and modulation data as judged by χ^2 analysis, it is likely that heterogeneity exists in dye rotation associated with the short and long rotational correlation times; if the data were sufficiently well-resolved, a model containing a bimodal distribution of rotational correlation times might be superior. Furthermore, it must be recognized that the measured fluid-phase cytoplasmic viscosity is valid only in aqueous compartments to which the solute is accessible; no direct information is available about the possible existence and properties of compartments that exclude solutes. If compartments that exclude solute do exist, then their physical properties are probably not important for cellular enzymatic and metabolic events. However, such compartments may act as additional obstacles that will further slow solute diffusion.

The translational motion of a small solute is governed by 3 factors: the instantaneous velocity of the solute when it is in motion, the fraction of time spent in motion, and the route between initial and final positions. The first factor is determined by an impediment to motion that acts over short time (or distance) scales, i.e., viscosity. The second factor is determined by the fraction of solute molecules that are bound (not in motion) at any instant in time. The third factor is determined by the solute trajectory in space, which depends upon the nature and distribution of obstacles. It is conceptually reasonable that (to a first approximation) binding is independent of viscosity and collisions. The results of the experiments in which glycerol was added to increase fluid-phase viscosity demonstrate experimentally that viscosity is independent of binding and collisions. Finally, solute-solvent interactions, which determine the viscosity, are much stronger than solute-solute interactions, which determine the collisional effects (Pusey and Tough, 1985). Factors 1 and 3 thus influence diffusion over very different time (or distance) scales and are largely independent of one another (Pusey and Tough, 1985). The good agreement between the product of the three factors that govern BCECF diffusion in cytoplasm, as determined independently, and the observed rate of BCECF diffusion,

provides further support for the separation of the overall barrier to diffusion into 3 independent components.

The translational motion of a small solute between an initial and a final position can be compared to the motion of an auto on a road, provinding useful heuristic insight into the factors that slow solute motion. The time required for an auto to reach a target destination depends on its speed, the fraction of time it is in motion, and its route. The auto's speed (assumed to be constant when the auto is in motion) is analogous to fluid-phase solute diffusion (F_1) driven by thermal energy. The fraction of time the auto is in motion (as opposed to stopped at red lights, etc.) is analogous to intracellular binding (F_2). Finally, the auto's route is analogous to the effects of obstacles (F_3), and can include traffic congestion (fluctuations in obstacle concentration) and cul-de-sacs (dead ends among immobile obstacles).

In addition, shortcomings in the solute/auto analogy provide useful insight into the differences between driven motion and random, diffusive motion. For the auto, the driver consciously chooses both the speed and the route, and can navigate the shortest distance between two points. However, the cost of this precision is that energy must be expended. For the Brownian solute, the speed is dictated by temperature and solvent viscosity, and the route traveled is random. The random route means that the time taken to travel between two points varies, and that the solute may not reach the second point at all. However, the advantage of this imprecision is that no energy must be expended. Brownian motion thus provides a cost-effective transport mechanism useful whenever precision and timing need not be exact.

The results and analyses reported in this study have direct relevance to other studies of the dynamics of solutes in crowded biological systems. A large body of related work has focused on the determinants of the diffusion of large molecules in the cytoplasm (reviewed by Luby-Phelps et al., 1988) as well as lipids (reviewed by Blackwell and Whitmarsh, 1990) and proteins (reviewed by Jacobson et al., 1987 and Scalettar and

Abney, 1991) in biological membranes. Membrane proteins provide a particularly striking example of hindered diffusion: their translation can be more than 100-fold slower in biological membranes than in dilute artificial membranes. Less than one-tenth of this decrease can be attributed to the factor herein called F_3 (Scalettar and Abney, 1991). The present study would suggest that this is not surprising and that F_1, F_2, and F_3, only when taken together, can account for the total decrease in protein mobility in biological membranes.

In summary, there are two principle conclusions to this study. First, the translational diffusion coefficient of a small solute (BCECF) in cytoplasm relative to that in water, D/D_0, is 0.27 ± 0.01. Second, this value can be modeled as a product ($D/D_0 = F_1F_2F_3 = 0.25 \pm 0.03$) of three independent factors reflecting increased fluid-phase cytoplasmic viscosity ($F_1 = 0.78$), BCECF binding to relatively immobile cellular components ($F_2 = 0.81$), and, most importantly, collisional interactions of BCECF with cytoplasmic components ($F_3 = 0.40$). Therefore, for a small metabolite-sized solute that does not bind to cellular components, the diffusion coefficient for long-range translation would be ~ 2×10^{-6} cm^2/s (Furukawa et al., 1991). The characteristic times associated with solute diffusion over 10 nm, 1 μm and 10 μm distances would thus be 80 ns, 800 ms, and 80 ms, respectively.

Chapter 3

TRACKING OF SINGLE FLUORESCENT PARTICLES IN 3 DIMENSIONS: USE OF CYLINDRICAL OPTICS TO ENCODE PARTICLE POSITION

3.1 Summary

We present a novel optical technique for three dimensional tracking of single fluorescent particles using a modified epifluorescence microscope containing a weak cylindrical lens in the detection optics and a microstepper-controlled fine focus. Images of small, fluorescent particles were circular in focus but ellipsoidal above and below focus; the major axis of the ellipsoid shifted by 90° in going through focus. Particle z position was determined from the image shape and orientation by applying a peak detection algorithm to image projections along the x and y axes; x,y position was determined from the centroid of the particle image. Typical spatial resolution was 12 nm along the optical axis and 5 nm in the image plane with a maximum sampling rate of 3-4 Hz. The method was applied to track fluorescent particles in artificial solutions and living cells. In a solution of viscosity 30 cP, the mean squared distance (MSD) traveled by a 264 nm diameter rhodamine-labeled bead was linear with time to 20 s. The measured diffusion coefficient, 0.0558 ± 0.001 $\mu m^2/s$ (SE, n= 4), agreed with the theoretical value of 0.0556 $\mu m^2/s$. Statistical variability of MSD curves for a freely diffusing bead was in quantitative agreement with Monte Carlo simulations of 3 dimensional random walks. In a porous glass matrix, the MSD data was curvilinear and showed reduced bead diffusion. In cytoplasm of Swiss 3T3 fibroblasts, bead diffusion was restricted. The water permeability in individual Chinese Hamster Ovary cells was measured from the z movement of a fluorescent bead fixed at the cell surface in

response osmotic gradients; water permeability was increased by >3-fold in cells expressing CHIP28 water channels. The simplicity and precision of this tracking method may be useful to quantify the complex trajectories of fluorescent particles in living cells.

3.2 Introduction

Single particle tracking (SPT) is a unique approach to monitor the directed and diffusive motions of individual particles in cellular compartments. Unlike fluorescence photobleaching recovery and autocorrelation spectroscopy, SPT provides information about the dynamics of single particle motion rather than ensemble-averaged information about populations of particles (Qian et al., 1991; Zhang et al., 1993). By analysis of particle trajectories, components of directed, diffusive and restricted motion can in principle be resolved, and a direction can be assigned to the average motion of the particle (Sheetz et al., 1989).

Previous SPT studies have been limited to analysis of particle trajectory in two dimensional systems. In general, a temporal series of images of small fluorescent or gold particles was analyzed to generate a series of x, y particle coordinates. Because only x and y were measured, SPT has been applied mainly for the analysis of the molecular mobility of proteins in 2D systems such as plasma membranes. Using gold-tagged concanavalin A in the plasma membrane of macrophages, Sheetz et al. (1989) reported that single receptors exhibited both random diffusive motion and directed motion at different times. Gross and Webb (1983) also observed random and directed mobility states for both individual molecules and clusters of fluorescently-labeled LDL receptors on the surface of human fibroblasts. Two dimensional SPT has also been applied to the analysis of kinesin movement in microtubules (Gelles et al., 1988), mitochondrial motion in liver cells (Salmeen et al., 1985), and cytoplasmic diffusion of gold particles (Geerts et al., 1987). The systems for these studies were either two dimensional or two dimensional projections

of a three dimensional system. A complete analysis of particle mobility in three dimensional specimens requires determination of x, y and z positions.

Several types of biological applications require three dimensional SPT (3D SPT). By analogy to SPT studies of molecular diffusion in the plasma membrane, the three dimensional motion of particles within the cytoplasm should be measurable. Intracellular traffic patterns could be monitored from the trajectories of labeled intracellular organelles or other subcellular components. Changes in cell shape and local cell membrane motion could be followed from the trajectories of immobilized particles at the cell surface.

We present a novel optical technique for 3D SPT of fluorescent particles in biological samples in real time. The technique is simple to implement and its principle is applicable to other types of microscopy, including differential interference contrast microscopy. The three dimensional position of a particle was encoded into its image by introducing a weak cylindrical lens into the optical detection path. Computer analysis of the shape, orientation and position of the particle's image was applied to retrieve the x, y and z coordinates. The 3D trajectory was then reconstructed from analysis of a temporal series of images. The spatial resolution and optical requirements of the SPT instrument were evaluated, and applications in model and biological specimens are presented.

3.3 Materials and Methods

Optical Instrumentation

An epifluorescence microscope (Diaplan, Leitz, Rochleigh, NJ) was modified to carry out 3D SPT by incorporation of a cylindrical lens and microstepper motor; the computer algorithms to determine three-dimensional position are described in the Image Analysis section. Fluorescence was excited with a stabilized 100 W Hg-Xe arc lamp, 530±20 interference filter and 560 nm dichroic mirror, and detected through a 590 nm barrier filter. A long focal length cylindrical lens (focal length: 560 cm, J. L. Woods

Optical Systems, Santa Ana, CA) was positioned in the detection path 15 mm beyond the exit aperture of the objective lens (Nikon CF Plan Apochromat 60 X/1.40 NA oil immersion). When viewed through this optical arrangement, a small particle appeared either ellipsoidal or circular depending upon its z position.

Images were collected by a charge coupled device (CCD) camera (AT200 series; Photometrics Ltd., Tucson, AZ) with a TK512CB CCD chip (Tektronix Inc.; Beaverton, OR) contained within a camera housing cooled to -40° C (CH250; Photometrics). Images were digitized into a 512 x 512 pixel array at 14 bit resolution. Details of the optoelectronic characteristics of this camera were described previously (Zen et al, 1992). The axis of the cylindrical lens was aligned parallel to the rows of the CCD array. Pixel array size at the object plane with the 60 X objective lens and cylindrical lens was 261 x 263 nm.

The z position of the stage was controlled using a microstepper motor (Model CX indexer/drive unit with C57-51 motor 12,800 steps/revolution; Compumotor Corp., Petaluma, CA) driving the fine focus control with a hard rubber coupling. The stage could be moved in 25 nm z increments. The vertical position of the microscope stage and image acquisition were controlled from a 25 MHz 486DX PC computer using software custom-written in Microsoft C 7.0. Software is available on request.

Analysis of Particle Position

The mean squared displacement (MSD) vs time relation was calculated for a particle trajectory as described by Qian et al. (1991). At times $t = n\Delta T$ (n=0, 1, 2,...) where ΔT is the sampling period, MSD [$\rho(t)$] and MSD along each axis, [$\rho_x(t)$, $\rho_y(t)$, $\rho_z(t)$], were calculated by,

$$\rho_x(t) = \frac{1}{N}\sum_{i=1}^{N}(x_{i+n} - x_i)^2 \qquad \rho_y(t) = \frac{1}{N}\sum_{i=1}^{N}(y_{i+n} - y_i)^2 \qquad \rho_z(t) = \frac{1}{N}\sum_{i=1}^{N}(z_{i+n} - z_i)^2$$

(3-1a)

$$\rho(t) = \rho_x(t) + \rho_y(t) + \rho_z(t) \quad (3\text{-}1b)$$

where N is the total number of positions recorded in the sequence. The diffusion coefficient, D, of the particle in three dimensions was calculated from the slope of the linear portion of a plot of $\rho(t)$ vs t using the equation, $D = \rho(t)/6t$.

For some measured particle trajectories, there were discontinuities in the trajectory sequence because of required adjustments in the z position of the microscope stage (see Image Analysis). A continuous sequence was generated for analysis by Eqs. (3-1) by excluding these discontinuities from the sequence and adjusting the remaining positions and times of the sequence to account for the excluded point.

Preparation of Artificial Samples

Two types of samples were prepared based on the method of Hiraoka et al (1990): samples containing immobilized fluorescent beads mounted within a liquid test specimen, and samples containing freely diffusing fluorescent beads. Red fluorescent latex beads (264 ± 9 [SD] nm diameter, excitation: 580 nm, emission: 605 nm) modified with surface sulfate groups (Molecular Probes, Eugene, OR) were used. To immobilize the beads at a depth of 0 μm into a liquid test specimen, beads were dried onto coverslips and 10 μL of glycerol was sandwiched between the coverslip and a larger glass slide so that the beads were in contact with the glycerol. The perimeter of the coverslip was sealed to the glass slide with clear nail enamel. To immobilize the beads at a specified depth, the procedure was reversed. Beads were dried onto a glass slide and a microliter volume of the test solution (calculated from coverslip area and the desired solution layer thickness) was sandwiched between the slide and coverslip. Examination of samples by brightfield confocal microscopy confirmed sample thickness and bead immobility.

To prepare samples containing freely diffusing beads, microliter volumes of a bead suspension in water-glycerol solutions were sandwiched between a glass slide and

coverslip to give a sample thickness of 30 μm. The sample was then sealed at the edges as above. To examine the effect of immobile barriers on bead diffusion, a fragment (≈ 5 x 5 mm) of porous glass filter (1.2 and 0.7 μm pore size, ≈ 250 μm thickness, Millipore Corp., Bedford, MA) was soaked in the bead-solution mixture for 1 min. The filter was placed between a coverslip and glass slide, excess bead-solution mixture was added, and slight pressure was applied to the cover slip to eliminate air bubbles. Viscosities of the water-glycerol solutions were determined from the published reference tables (Miner and Dalton, 1953).

Cell Culture

Swiss 3T3 fibroblasts (American Type Collection No. CL-101) were grown on 18-mm diameter round glass coverslips in DME-H21 supplemented with 5 % fetal calf serum, 100 U/ml penicillin and 100 μg/ml streptomycin. Cells were maintained at 37^{o} C in a 95 % air / 5 % CO_2 incubator and used before confluence. Coverslips were transferred to a 200 μL-perfusion chamber (to facilitate rapid buffer changes) in which the cell-free surface of the coverglass was accessible to the objective. Chinese hamster ovary (CHO) cells were transfected with cDNA encoding water channel CHIP28 using a mammalian expression vector with RSV promoter (Ma et al, 1993). Measurements were carried out 72 hours after transfection.

Bead Diffusion in Cell Cytoplasm

Red fluorescent latex beads (93 ± 7 [SD] nm diameter, excitation: 580 nm, emission: 605 nm) modified with surface carboxylate groups (Molecular Probes, Eugene, OR) were suspended in phosphate buffer saline (PBS) at 0.02 volume %. Microinjection pipettes were pulled from 0.9 mm ID borosilicate glass with omega dot fiber (FHC, Brunswick, ME) using a Kopf vertical pipette puller (David Kopf Instruments, Tujunga, CA). Approximately 5 fL of the suspension was microinjected into the cytoplasm of Swiss

3T3 fibroblasts using an Eppendorf microinjection apparatus (Microinjector 5242, Madison, WI).

Water Permeability in Individual Cultured Cells

To measure the water permeability of an individual cell, the z axis motion of 264 nm red fluorescent beads immobilized at the surface of CHO cells was measured in response to osmotic gradients. Cells were incubated with a PBS-bead solution (0.002 volume %) for 10 min at room temperature and then rinsed in PBS. The beads were immobilized on the cell surface at a density of ~1 bead/ 1000 μm^2. The z axis motion of a bead near the apex of the cell was measured in response to switching the perfusing medium rapidly between isosmolar (300 mOsm, PBS) and hypoosmolar (150 mOsm, 1:1 dilution of PBS with distilled water) buffers.

Computer Simulations

To evaluate the statistical variation of the MSD plots measured for random diffusion, 3D random walks for a single particle were computed numerically by a modification of the method reported by Lee et al (1991) for 2D diffusion. The random walks were generated on a cuboidal lattice whose spacing was arbitrarily selected as 10 nm. Trajectories started at the origin; at each particle position, one of six directions ($\pm x, \pm y, \pm z$) was selected randomly and particle position was moved to the adjacent lattice site in that direction. After every 100 such movements, the particle position was recorded. MSD plots for the simulated random walks with 100, 500 and 1500 recorded positions were computed by Eq. (3-1) for comparison with experimental data.

To simulate bead diffusion within cells (restricted diffusion), random walks were confined within a cube of specified size. At each particle position, the particle was moved to the randomly selected site only if that site was within the boundary of the cube; otherwise the particle was not moved.

3.4 Image Analysis

Encoding 3D position information into the image of a particle

To encode positional information into a particle's image, a weak cylindrical lens was introduced into the emission path of an epifluorescence microscope above the objective lens (Fig. 3.1 left). When a small, fluorescent particle was viewed through this microscope, either an ellipsoidal or a circular image was formed. The center of the image corresponded to the x and y positions of the particle. The orientation and shape of the image encoded the z position. If the particle's z position was in the focal plane, the image was smallest in size and circular in shape (Fig. 3.1 right). The images became larger and ellipsoidal away from the focal plane; the major axis of the ellipsoids formed above the focal plane was perpendicular to that formed below the focal plane. Images formed without the cylindrical lens were circular in shape (Fig. 3.1 right).

Algorithms for determination of x, y and z positions

To determine particle position in 3 dimensions, binned projections of pixel intensity along the x and y axes of the image were analyzed. For a binned projection, each element, P_k, represents the sum of all pixels across the k^{th} row or column of the image (Fig. 3.2 A),

$$P_k = \sum_{i=1}^{N} I_{i,k} \quad \text{or} \quad P_k = \sum_{j=1}^{N} I_{k,j} \tag{3-2}$$

where $I_{i,j}$ is the pixel intensity at the position (i, j) and N is the total number of pixels along either the rows or columns of the array. Binned projections, rather than the collected 2D arrays, were processed because they contained sufficient information to determine a particle's position and required remarkably less computation time for position determination in real-time.

For the algorithms described below, an area-weighted quadratic fit was utilized to determine the contour of a binned projection over a single pixel length. Area weighted

Figure 3.1. Asymmetry in images of a 264 nm red fluorescent latex bead produced by a cylindrical lens. The epifluorescence microscope was modified with a cylindrical lens and a microstepper motor for adjusting the z position of the stage (see text for details). Beads were imaged with a Nikon 60X oil immersion objective lens with n=1.48 immersion oil. Indicated z positions are relative to the focal plane. Images are shown in the presence (left) and absence (right) of the cylindrical lens in the microscope emission path.

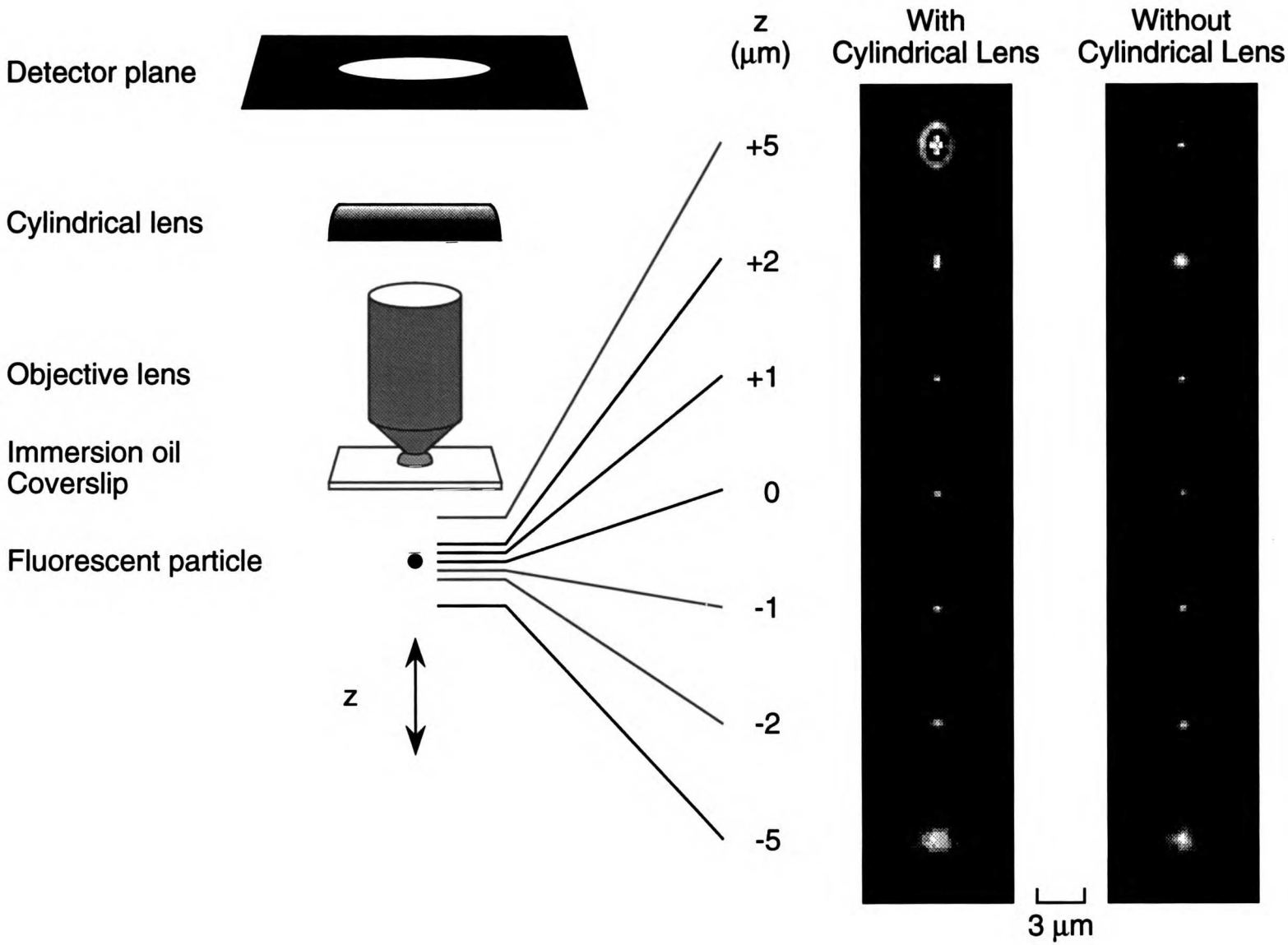
Detector plane
Cylindrical lens
Objective lens
Immersion oil
Coverslip
Fluorescent particle
z
z (μm)
+5
+2
+1
0
-1
-2
-5
With Cylindrical Lens
Without Cylindrical Lens
3 μm

Figure 3.2. Determination of z position from image asymmetry. A. Image width algorithm: The width, w, of the image along one axis was determined as the distance between the minimum and maximum of the derivative of the projection. **B.** Peak detection algorithm: The fitted contour of the binned projection, P(x), was multiplied by a peak detection function, $\Lambda(x)$. The area of the product, $\phi=\int P(x)\Lambda(x)\,dx$, as indicated by the shaded region, was used to calculate $\Phi(z)$ as defined in Eq. (3-6). **C** and **D.** Representative calibration curves for $w_x(z)$, $w_y(z)$, or $\Phi(z)$ for a fixed 264 nm red fluorescent bead. Each point represents the average of 5 images taken of the bead at that position; standard deviations are smaller than the circle size. Images were collected as in Fig. 3.1.

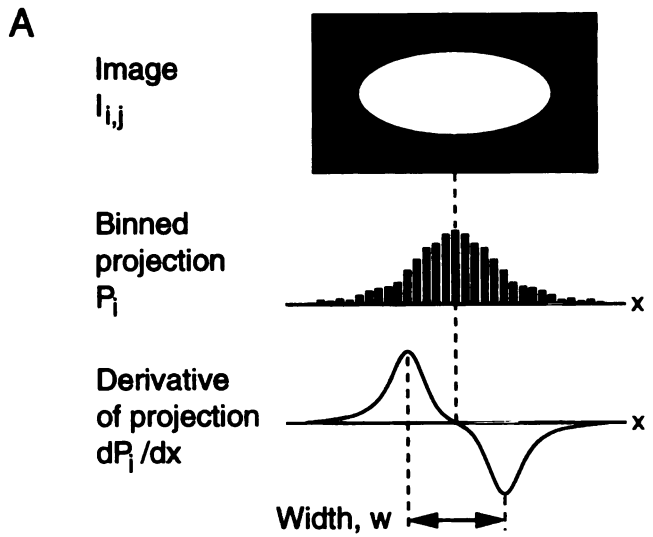
A
Image
$I_{i,j}$
Binned
projection
P_i
x
Derivative
of projection
dP_i/dx
x
Width, w

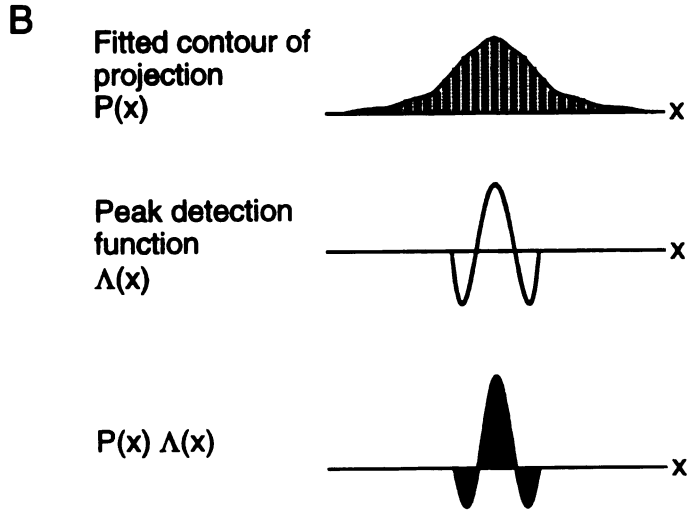
B
Fitted contour of
projection
P(x)
x
Peak detection
function
Λ(x)
x
P(x) Λ(x)
x

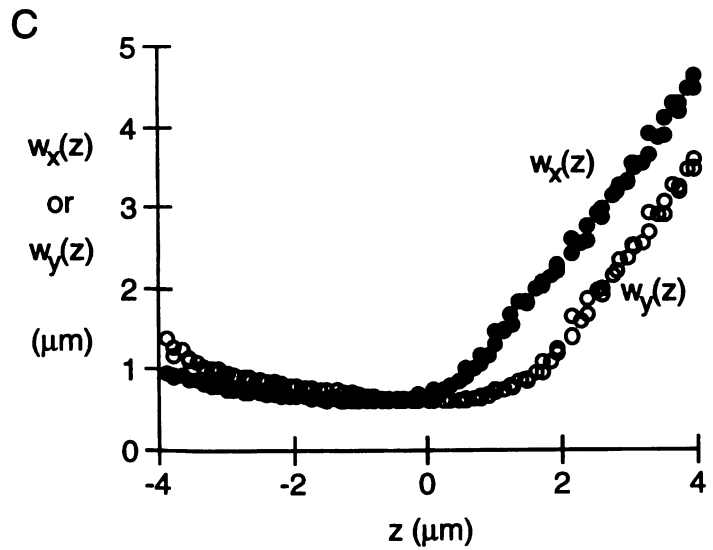
C
$w_x(z)$
or
$w_y(z)$
(μm)
5
4
3
2
1
0
$w_x(z)$
$w_y(z)$
-4
-2
0
2
4
z (μm)

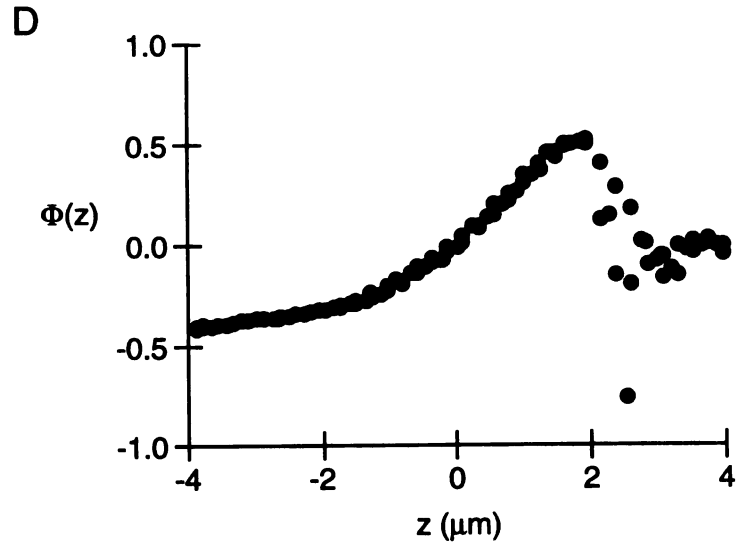
D
Φ(z)
1.0
0.5
0.0
-0.5
-1.0
-4
-2
0
2
4
z (μm)

fitting was used to construct a continuous contour because images were close to the pixel resolution of the camera (Inoué, 1986). As defined here, the coefficients, a_i, b_i, c_i, for the area weighted fit, $\zeta_i(x) = a_i x^2 + b_i x + c_i$, over 3 adjacent bins, may be expressed in terms of the bin values, P_{i-1}, P_i, P_{i+1}. Three linear equations are obtained from the integral of $\zeta_i(x)$ over each bin: $\int_0^1 a_i x^2 + b_i x + c\, dx = P_{i-1}$, $\int_1^2 a_i x^2 + b_i x + c\, dx = P_i$, and $\int_2^3 a_i x^2 + b_i x + c\, dx = P_{i+1}$. The solution of these equations for a_i, b_i, and c_i is:

$$\begin{bmatrix} a_i \\ b_i \\ c_i \end{bmatrix} = \frac{1}{6}\begin{bmatrix} 3 & -6 & 3 \\ -12 & 18 & -6 \\ 11 & -7 & 2 \end{bmatrix}\begin{bmatrix} P_{i-1} \\ P_i \\ P_{i+1} \end{bmatrix} \tag{3-3}$$

where x is defined in units of pixel lengths, and x=0 is at the left-most boundary of P_{i-1}. Because a_i, b_i and c_i best define the contour over the central bin, Eq. (3-3) was used only over the length of the central bin, P_i.

For determination of x and y coordinates, the position of the maximum in the contour of each projection was determined. At the bin with the highest summed intensity, an area-weighted quadratic fit [Eq. (3-3)] was applied. The position at the maximum of the quadratic fit, $-b_i/2a_i$, was taken as the position of the bead along that axis. The position of this maximum was insensitive to image intensity and offset.

For determination of z position, two algorithms were applied to detect the spread in the distribution of each projection. The first algorithm was designed to detect projection differences for large ellipsoidal images generated far from the focal plane. The second algorithm was designed to detect differences for smaller ellipsoids generated near the focal plane.

The first algorithm for z position utilized the width of a binned projection along each axis (Fig. 3.2 A). The width, w, was calculated as the distance between the

maximum and minimum derivatives of the P_i projection. The numerical derivative of the projection was calculated as (James et al, 1985),

$$\left.\frac{dP}{dx}\right|_{x=i} \approx (P_{i-2} - 8P_{i-1} + 8P_{i+1} - P_{i+2})/12 \qquad (3\text{-}4)$$

where x is the projection position, in pixel lengths. The positions of the minimum and maximum in the derivative profile were determined from area-weighted quadratic fits [Eq. (3-3)] applied at the minimum and maximum in the derivative profile. The widths of the projection along each axis, $w_x(z)$ and $w_y(z)$, differed when the particle was not at the focal plane because of the ellipticity of the image. $w_x(z)$, $w_y(z)$, and their relative magnitudes were used to determine z position (see below). Because only the first derivative of the projection was analyzed, image intensity and offset had little effect on the measured width of the projections.

The second algorithm for z position applied one-dimensional peak detection to the projection for each axis. This algorithm is based on edge detection functions employed in digital image processing (Gonzalez and Wintz, 1987). The peak detection function must be convex in shape, with only a single maximum flanked by 2 minima, and have a total integrated area of 0 (Fig. 3.2 B). The single peak detection function, $\Lambda(x) = (16\text{-}x^2)(16\text{-}5x^2)/256$, where x is in pixel lengths, was chosen to satisfy these properties. Peak detection was implemented by aligning the maximum of $\Lambda(x)$ with the maximum of the continuous contour of the binned projection, P(x) (Fig. 3.2 B). The product of the two functions was then integrated from pixels -4 to +4. P(x) was not determined as a continuous function, but as a set of fitted quadratic polynomials for each pixel, $\zeta_i(x)$, whose coefficients are defined by Eq. (3-3). The integral was evaluated as a discrete sum of integrals,

$$\phi = \int_{-4}^{+4} \Lambda(x)P(x)\,dx \approx \sum_{i=-4}^{3} \int_{x=i}^{x=i+1} \Lambda(x)\zeta_i(x)\,dx$$
$$= \sum_{i=-4}^{3} \int_{x=i}^{x=i+1} \left[\frac{1}{256}\left(16-x^2\right)\left(16-5x^2\right)\right]\left[a_i(x-i+1)^2 + b_i(x-i+1) + c_i\right] dx \qquad (3\text{-}5)$$

where x is the projection position in pixel lengths and x=0 is defined as the center of the projection. The parameter, ϕ, is a measure of the spread of the projection distribution near the center of the projection. ϕ was maximum when the spread of the projection was small and decreased as the spread increased. The value of ϕ for the x and y projections, ϕ_x and ϕ_y, differed when the particle was not in the focal plane because of the elliptical shape of the image, as quantified by the function $\Phi(z)$,

$$\Phi(z) = \left(\phi_y(z) - \phi_x(z)\right) / \left(\phi_y(z) + \phi_x(z)\right) \qquad (3\text{-}6)$$

Measurement of z Position Utilizing Calibration Data

Calibration curves [$w_x(z)$, $w_y(z)$ and $\Phi(z)$] measured prior to an experiment were used to determine z position. Calibration data was collected using a single immobilized reference bead with the same diameter as that used for subsequent SPT measurements. At 50 z positions from 5.75 μm below to 5.75 μm above the focal plane, five images of the single bead in each z plane were acquired. The average values and standard deviations for $w_x(z)$, $w_y(z)$ and $\Phi(z)$ of the 5 images were calculated. Calibration data consisted of 3-5 sets of measurements, each for 50 z positions. To change the z position of the bead during collection of calibration data, the microscope stage was raised in steps of 0.23 μm; only upward steps were used to minimize errors from mechanical hysteresis of the fine focus control. Because of this hysteresis, the exact z position of the focal plane was determined by $\Phi(z)$ rather than from the absolute angular position of the motor shaft (see Discussion). All z positions for the calibration were reported relative to the focal plane (z=0).

Representative calibration data for $w_x(z)$, $w_y(z)$ and $\Phi(z)$ are shown in Figs. 3.2 C and 3.2 D. Both $w_x(z)$ and $w_y(z)$ reach minima; however, the minima were located at different positions on the z axis because the cylindrical lens magnifies along one axis only. $\Phi(z)$ monotonically increased as z position increased from -3 μm to +2 μm. $\Phi(z)$ did not increase beyond +2 μm because of the appearance of rings in the image (Fig. 3.1 right). The z focal plane position was determined based on the image symmetry ($\Phi(z) = 0$) at the focal plane. For each set of 50 z positions measured, $\Phi(z)$ was solved using a fifth order polynomial fitted to the 5 calibration data points centered at the focal plane.

During an experiment, z position was determined in real time from the values of $w_x(z)$, $w_y(z)$ and $\Phi(z)$ for a single image using the calibration curves. z position was first estimated as the average of the $w_x(z)$ and $w_y(z)$ estimates. If the bead was between -2 and 1.8 μm of the focal plane, a more accurate determination of z position was provided by $\Phi(z)$. If the bead was outside of the z=-2 to 1.8 μm region, the microstepper motor was used to position the bead to within 1 μm of the focal plane. The time required to reposition the bead was < 0.5 s; particle tracking was not continued until 1 s after motor movement to reduce transient mechanical phenomena (such as shifting of the immersion oil).

Procedure for continuous 3D particle tracking

The 3D trajectory of a particle was determined in real time by applying the algorithms described above to a sequence of images. Prior to an experiment, calibration curves were measured. At the beginning of an experiment, a small rectangle (≈ 30 x 30 pixels) of the CCD array was selected which contained the particle to be tracked. An image was collected at an exposure time of 50 ms and analyzed to determine x,y,z position. The z position of the microscope stage was adjusted if the particle's z position was outside of the -2 and 1.8 μm range. The location of the rectangle on the CCD array was adjusted if particle's x or y positions were within 7 pixels of the boundary of the image. For analysis of particle trajectory, z positions were determined using $\Phi(z)$ (from -2 to 1.8 μm).

3.5 Results

Precision and Errors in 3D position measurement

Position measurements on immobilized beads were carried out to evaluate instrument precision. Factors which influence measurement precision include microscope vibration, mechanical stage drift, and detector signal and noise amplitudes. To estimate the standard deviations for position determination, σ_x, σ_y, and σ_z, the position of an immobilized bead located at z positions within 2 μm of the focal plane was measured. For random noise, $\rho^2(\Delta t)$ for an immobilized bead should be time-independent and equal to $2(\sigma_x^2+\sigma_y^2+\sigma_z^2)$ for $\Delta t>0$; $\rho_x^2(\Delta t)$, $\rho_y^2(\Delta t)$ and $\rho_z^2(\Delta t)$ are also time-independent and equal to $2\sigma_x^2$, $2\sigma_y^2$ and $2\sigma_z^2$, respectively (Couch, 1987). The measured MSD plots shown in Fig. 3.3 A for a single z position are time-independent as predicted. The measurement errors for each axis as a function of z position are shown in Fig. 3.3 B. Errors along x and y showed little change in going from -2 to 1.8 μm around focus. Errors along z were greatest at -2 and 1.8 μm from focus because of the decreased image intensity and the low slope of $\Phi(z)$ at these positions. Minimum z error occurred at $z \approx 1$ μm above focus where spatial resolution, image intensity and the slope of $\Phi(z)$ are optimum. Typical measurement SD (precision) was 5 nm along x, 2-3 nm along y and 12 nm along z. It should be noted that these errors are much smaller than the scatter observed in $w_x(z)$, $w_y(z)$, and $\Phi(z)$ (Figs. 3.2 C, D). This scatter represents not the precision of the technique, but the composite effects of mechanical hysteresis and gear lash on the accuracy which limited the accuracy of z position determination. Because of this variability, many calibration data points were measured to construct the calibration curves.

The refractive index of the medium between the particle and objective lens affects the image formation properties of the microscope system (Gibson and Lanni, 1991). As a particle moves in the z direction within a sample, its calibration curves [$w_x(z)$, $w_y(z)$, and $\Phi(z)$] may change and introduce uncertainty in z position determination. To evaluate the effects of refractive index and sample thickness in our system, $w_x(z)$, $w_y(z)$ and $\Phi(z)$ were

Figure 3.3. Measurement accuracy in 3D SPT. A. Representative MSD curves for an immobilized 264 nm fluorescent bead located in the focal plane. **B.** σ_x, σ_y, and σ_z, as a function of z. Each point was determined from a trajectory ≈ 600 steps sampled at a rate of ≈ 2 Hz. **C** and **D.** Dependence of $\Phi(z)$ for a bead immobilized at 0 μm and 20 μm into water (n=1.33) (C) and 83 % glycerol in water (n=1.44) (D). Images were collected as in Fig. 3.1.

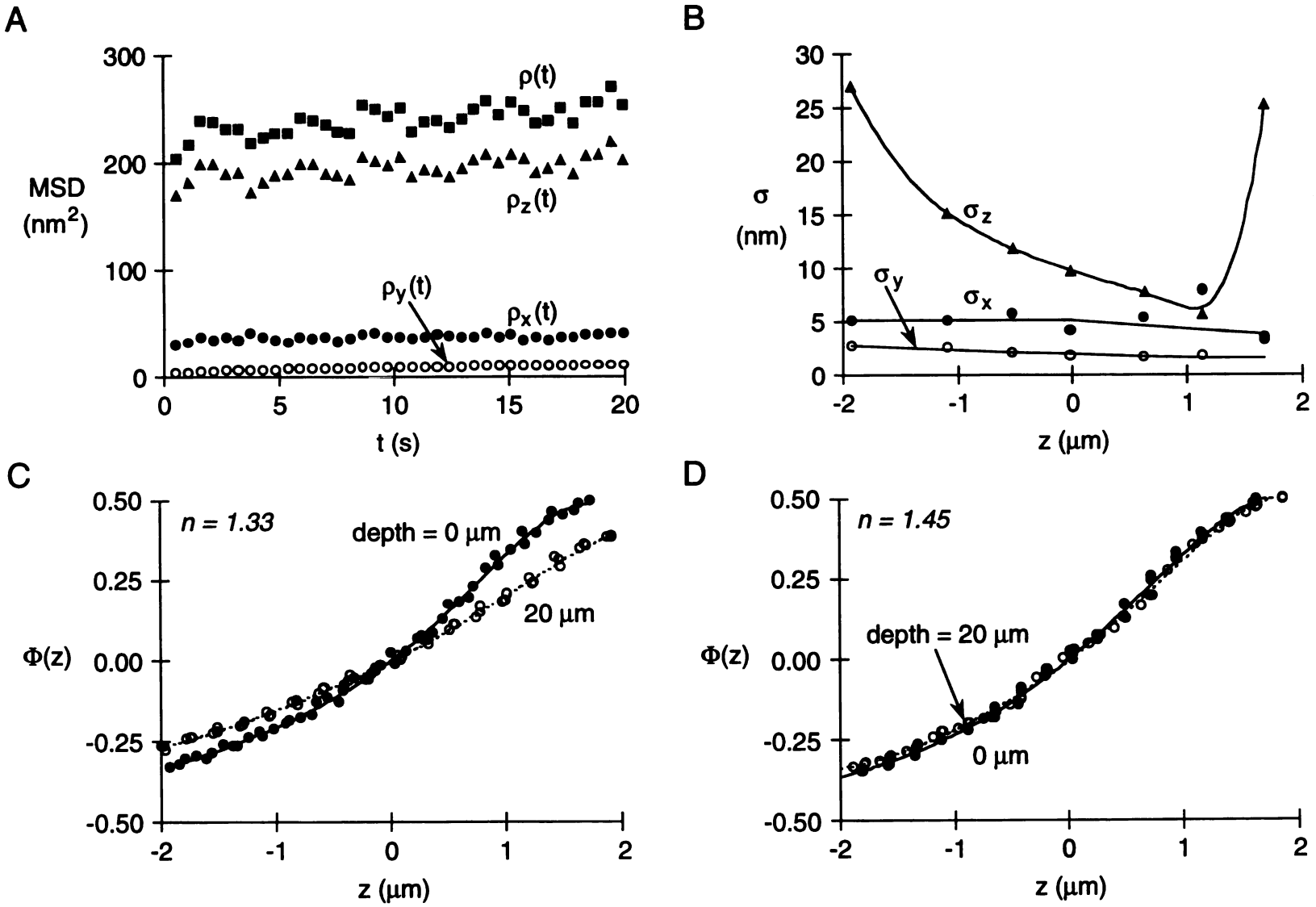
A
300
200
100
0
MSD
(nm²)
ρ(t)
ρz(t)
ρy(t)
ρx(t)
0
5
10
15
20
t (s)
B
30
25
20
15
10
5
0
σ
(nm)
σz
σy
σx
-2
-1
0
1
2
z (μm)
C
0.50
0.25
0.00
-0.25
-0.50
Φ(z)
n = 1.33
depth = 0 μm
20 μm
-2
-1
0
1
2
z (μm)
D
0.50
0.25
0.00
-0.25
-0.50
Φ(z)
n = 1.45
depth = 20 μm
0 μm
-2
-1
0
1
2
z (μm)

measured for beads immobilized at 0 and 20 μm depths in water (n=1.33) and 83 % aqueous-glycerol (n=1.45) solution. The lens immersion fluid had a refractive index of 1.48. For the water sample, the shape of the $\Phi(z)$ changed significantly for bead depths of 0 and 20 μm (Fig. 3.3 C). However, in the glycerol solution, the shape of $\Phi(z)$ showed little change (Fig. 3.3 D), suggesting that changes in the calibration curves with z position are small if the refractive indices of the sample and immersion oil are similar. The same conclusion was obtained from analysis of the $w_x(z)$ and $w_y(z)$ curves (not shown). For the diffusion measurements reported below, the instrument was calibrated using an immersion oil having a refractive index of 1.48, which was close to that of the sample media (1.44-1.45).

SPT of Small Beads in Artificial Systems

Fig. 3.4 A shows two representative trajectories of a small fluorescent latex bead in an aqueous solution containing 83 % glycerol. The trajectories appeared to be random along all three axes. To determine whether these trajectories corresponded to random diffusive motion, MSD plots along the x, y, and z axes were constructed from a series of 1800 positions recorded every 0.54 s (Fig. 3.4 B). The plots were linear and overlapped over the first 5 s, suggesting that the particle diffused randomly in three dimensions. The divergence of the MSD plots beyond 5 s was due to statistical variability of random walks.

$\rho(t)$ (in three dimensions) corresponding to the data provided in Fig. 3.4 B was linear from 0-20 s (Fig. 3.4 C). From the slope (see Methods), the diffusion coefficients for beads in water-glycerol solutions of viscosities 30 and 56 cP were 0.0558 ± 0.001 (SE, n=4) and 0.0232 ± 0.001 (SE, n=4) $\mu m^2/s$, respectively. For the conditions of our experiments (27.5° C, particle radius=264 nm), the Stokes-Einstein equation predicts diffusion coefficients of 0.0556 and 0.0295 $\mu m^2/s$, respectively, in agreement with the measured values.

Figure 3.4. Three dimensional SPT of beads in water-glycerol solutions and porous glass filters. The 3D position of a 264 nm red fluorescent particle was measured every 0.54 seconds for 15 min. **A.** 100 steps of two 3D trajectories of a freely diffusing particle in an 83 % aqueous glycerol solution having viscosity 60 cP at 27.5° C. Projections of trajectories onto the x-y and x-z plane are shown. Arrows indicate the initial bead positions. **B.** Representative MSD plots for a freely diffusing particle in a 77 % aqueous glycerol solution of viscosity 30. **C.** Representative $\rho(t)$ curves for a freely diffusing particle in 77 % and 83 % aqueous glycerol solutions having viscosities 30 and 56 cP, respectively. **D.** Representative $\rho(t)$ plots for a freely diffusing particle in free solution and in porous glass filters with 1.2 and 0.7 μm pore sizes.

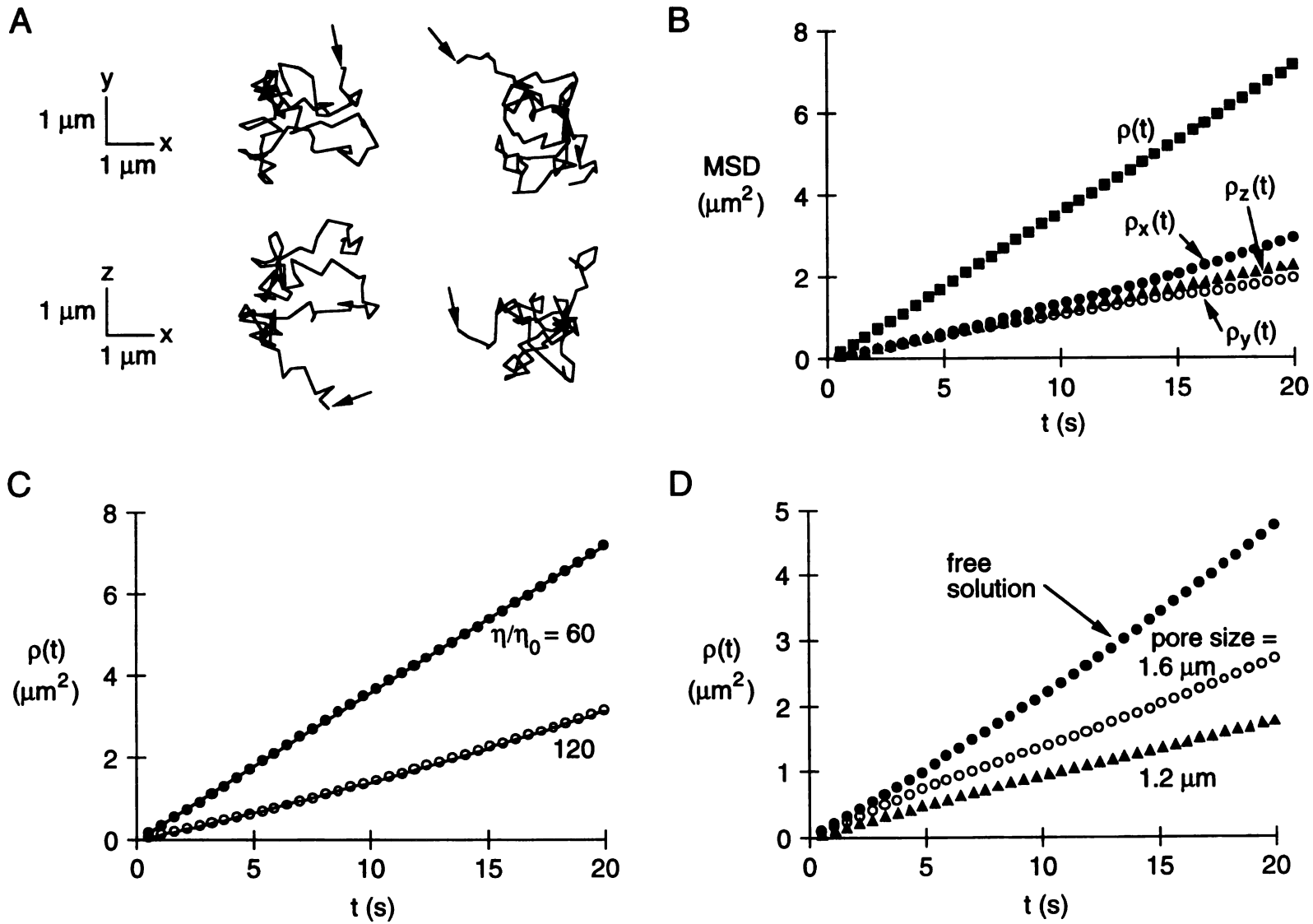
A
y
1 μm
x
1 μm
z
1 μm
x
1 μm
B
MSD
(μm²)
ρ(t)
ρz(t)
ρx(t)
ρy(t)
t (s)
C
ρ(t)
(μm²)
η/η0 = 60
120
t (s)
D
ρ(t)
(μm²)
free
solution
pore size =
1.6 μm
1.2 μm
t (s)

Similar 3D SPT studies were carried out for bead diffusion in porous glass filters (1.2 and 0.7 μm pore sizes) soaked in a water-glycerol solution of viscosity 56 cP (Fig. 3.4 D). $\rho(t)$ decreased from its value in free solution as pore size decreased. The shape of $\rho(t)$ for particle diffusion in the filters demonstrated two regions: an increasing nearly linear region from 0 to ~5 s, and a linear region with decreased slope at >5 s. These regions probably correspond to short and long range bead diffusion in the restricted environment. Qualitatively similar results were computed by Saxton (1989) for Monte Carlo simulations of mobile point particles diffusing in a two dimensional lattice containing immobile obstacles, and by Pusey et al (1979) for the self-diffusion of microspheres in concentrated solutions.

Computer Simulations of Diffusion in Free Solution

To compare measured MSD plots with theory, Monte Carlo simulations were carried out as described in Methods. As the trajectory length of the random walk was increased, $\rho(t)$ became more linear, similar to results computed for 2D diffusion (Qian et al., 1991) (Fig. 3.5 A). For each plot, $\rho_x(t)$, $\rho_y(t)$, $\rho_z(t)$ were colinear for the first few time intervals, after which time they diverged (data not shown). These plots are not predicted to be linear nor overlapping at larger t because a finite number of data points were collected.

The MSD plots for a simulated 3D random walk (Fig. 3.5 A) had the same qualitative shape as those determined experimentally for bead diffusion in free solution (Figs. 3.4 B, C). Variabilities of each point in the $\rho_x(t)$, $\rho_y(t)$, $\rho_z(t)$ and $\rho(t)$ plots for the simulated trajectory were in quantitative agreement with those measured for random bead diffusion (Fig. 3.5 B). These results support the conclusion that the particles in our samples diffused randomly in all three dimensions and that the measurement uncertainties introduced by the tracking algorithms were small compared to the intrinsic statistical variability in 3D particle trajectories.

Figure 3.5. Computer simulations of MSD plots for 3D particle diffusion. **A.** $\rho(t)$ for computer simulated random walks of 100, 500 and 1500 steps in length. Step size was adjusted to give the same diffusion coefficient as that for a 264 nm bead freely diffusing in a 77 % aqueous glycerol (viscosity 30 cP). **B.** The ratio of the standard error to mean value for $\rho_x(t)$, $\rho_y(t)$, $\rho_z(t)$ and $\rho(t)$. Standard error was calculated for the set of squared distances used to determine the mean. Curves are shown for a computer simulated random walk and a measured 3D trajectory of a freely diffusing 264 nm bead having 1500 steps in length.

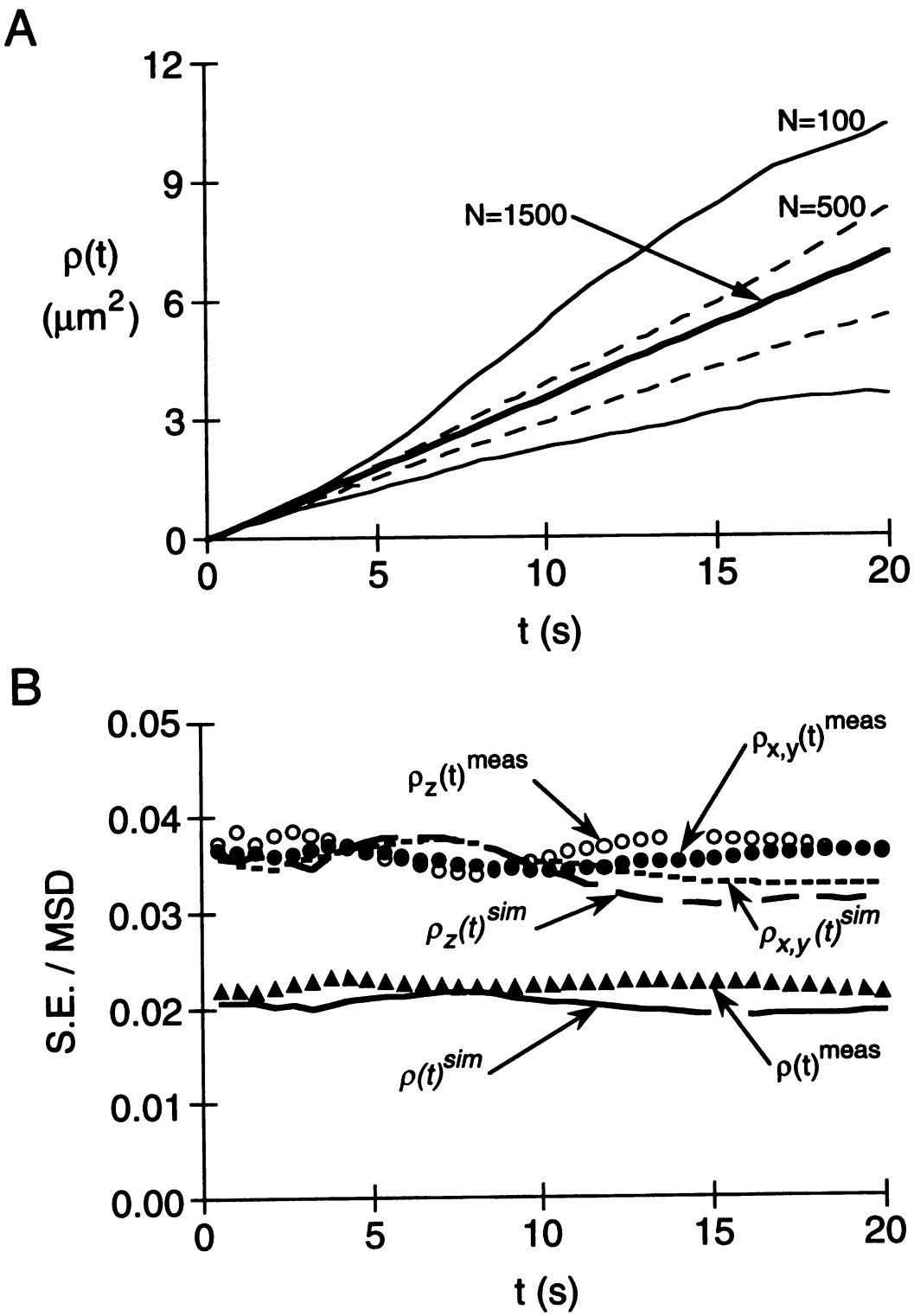
A
12
9
6
3
0
ρ(t)
(μm²)
N=100
N=500
N=1500
0
5
10
15
20
t (s)
B
0.05
0.04
0.03
0.02
0.01
0.00
S.E. / MSD
ρz(t)meas
ρx,y(t)meas
ρz(t)sim
ρx,y(t)sim
ρ(t)sim
ρ(t)meas
0
5
10
15
20
t (s)

SPT of Small Beads in Living Cells

Two applications of 3D tracking in living cells were demonstrated: bead diffusion in cytoplasm, and measurement of cell volume changes by the motion of beads at the cell surface. Small fluorescent latex beads (93 nm diameter) were microinjected into the cytoplasm of Swiss 3T3 fibroblasts and their 3D trajectories were measured. Following microinjection, the beads were confined to small pockets the cell, within which the beads diffused rapidly. These pockets decreased slowly in size following microinjection; after 2-3 hours, most beads appeared to be immobile. This rapid and confined motion is demonstrated by a representative MSD plots shown in Fig. 3.6 A (filled circles). The downward curvature of $\rho(t)$ indicates of particle diffusion either within a confined volume or in an obstacle-filled environment (Saxton, 1987; 1989). The shape of this curve was qualitatively similar to that for a random walk confined within a cube with side length 0.25 μm (curve b). Quantitative values for bead diffusion coefficients in cell cytoplasm cannot be deduced from this data because of the sampling rate of our instrument was not fast enough to measure the initial slope of the MSD plot.

Changes in cell volume were monitored from the z position of a small bead immobilized on the external surface of the cell plasma membrane. Three types of cells were compared: CHIP28-expressing CHO cells obtained by transient transfection with cDNA encoding CHIP28 water channels, non-expressing cells that did not incorporate the cDNA, and non-transfected (control) cells that were never exposed to the CHIP28 cDNA. In the absence of osmotic driving forces (perfusion with 300 mOsm solution), bead z position was constant (Fig. 3.6 B). In response to a 150 mOsm perfusing solution, cell volume (and bead z position) increased because of osmotic water influx; cell volume (and bead z position) decreased when solution osmolality was returned to 300 mOsm. Osmotic water permeability in CHIP28-expressing cells was remarkably higher than in the non-expressing and non-transfected cells as shown by the rate of z position change in response to an osmotic gradient. In four sets of experiments, the rate was increased by an average of 3.2-

Figure 3.6. Applications of 3D SPT in living cells. A. MSD plot for a bead microinjected into the cytoplasm of a Swiss 3T3 fibroblast (filled circles). Solid lines are MSD plots for a computer-simulated random walk confined within a cube with side a) 0.50 μm, b) 0.25 μm, and c) 0.10 μm. Both simulated and measured trajectories were 1166 steps in length. **B.** Measurement of osmotic water permeability in non-transfected and transfected CHO cells. The z position of a fluorescent bead immobilized at the cell surface was measured in response to perfusion with buffer of indicated osmolalities.

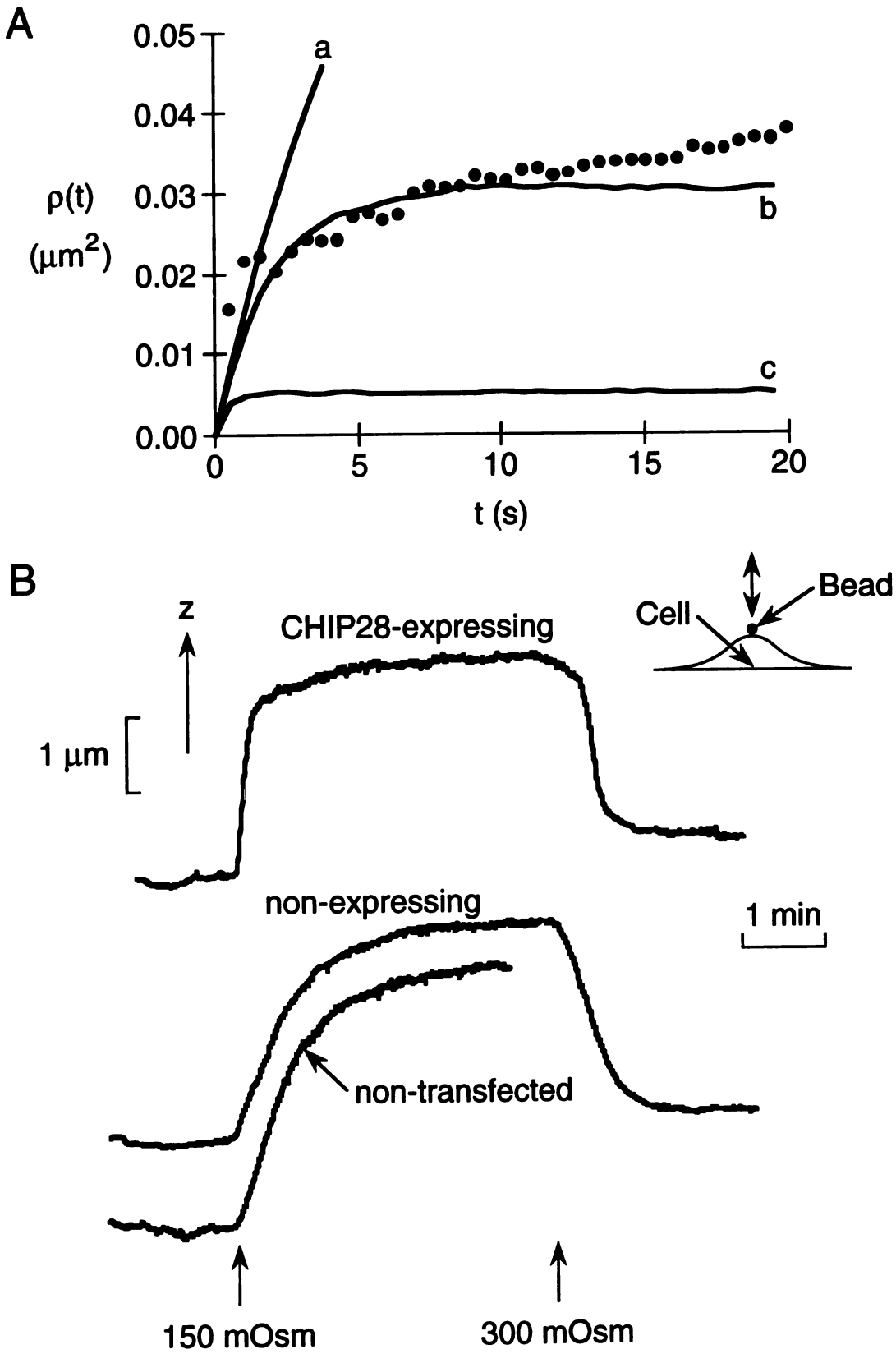
A
0.05
0.04
0.03
0.02
0.01
0.00
ρ(t)
(μm²)
a
b
c
0
5
10
15
20
t (s)
B
z
1 μm
CHIP28-expressing
Cell
Bead
non-expressing
1 min
non-transfected
150 mOsm
300 mOsm

fold.

3.6 Discussion

This study demonstrated three dimensional tracking of single fluorescent particles using a weak cylindrical lens introduced into the detection path of an epifluorescence microscope. The resulting images contained a focus-dependent asymmetry which encoded particle x, y and z coordinates. The transverse (x, y) coordinates were taken as the centroid of the image and the axial (z) coordinate was computed in real-time from the degree and orientation of the image. Two algorithms were developed to analyze particle z position in real time. The first algorithm determined the projection width, and the second applied one dimensional peak detection. z position was determined from algorithm parameters using calibration curves for an immobilized reference bead established at the beginning of an experiment. A focus-drive motor kept the in-focus plane close enough to the fluorescent particle so that the z-axis determination was accurate and unambiguous. The x, y coordinates of a particle were generally measured to within 5 nm and the z coordinate was measured to within 12 nm.

A distinct advantage of the astigmatic aberration produced by the cylindrical lens is the alignment of the focus-dependent asymmetry with the rows and columns of the detector array. Every microscope objective contains some degree of focus-dependent spherical aberration which could potentially be used to deduce z position. However, these aberrations are dependent upon the microscope objective and quantification of any asymmetries may require complex image recognition algorithms. With the cylindrical lens, the aberration is independent of the objective and, because of the alignment of the asymmetry with the detector array, quantification of the asymmetry is simple and rapid. The potential disadvantage of introducing astigmatic aberration is the degradation of the transverse (x,y) microscope resolution. This is apparent from a size comparison of the in-

focus images with and without the cylindrical lens (Fig. 3.1). With the cylindrical lens, the full width half maximum of the image is ≈ 0.3 μm, whereas without the lens, it becomes ≈ 0.5 μm. If the particle images remain well separated, the main effect of the image degradation is to decrease the overall brightness of the image.

To measure z position accurately, the calibration curves established for an immobile particle must remain valid as the particle moves within a sample. From the theoretical analysis of Gibson and Lanni (1991), particle images produced out-of-focus are independent of the particle z position when the refractive index of the immersion oil matches that of the sample. The independence of $\Phi(z)$ on particle z position was confirmed by direct measurement in Fig. 3.3 B. For our experiments on diffusion of beads in model systems, the refractive indices were closely matched; the z measurements were accurate as demonstrated by the colinearity of $\rho_x(t)$, $\rho_y(t)$, $\rho_z(t)$ in the random diffusion measurements (Fig. 3.4 B). The analysis of Gibson and Lanni may be extended to a general requirement that the refractive index of the immersion medium in contact with an objective lens must equal that of the sample. However, the refractive index of the immersion medium should be close its recommended value to minimize degradations in image contrast and resolution (Gibson and Lanni, 1991). Hence, for experiments involving biological samples, a water immersion objective lens would be best because the refractive index of these samples is close to that of water. Air and oil objectives could be used if appropriate correction factors are included in the calibration curves.

The precision to which the x, y, z position of a particle could be resolved was limited by the signal-to-noise ratio of the image. Factors which reduced the signal-to-noise ratio included instrument microvibration, detector dark counts and read noise, low image intensities, and image smearing because of the non-zero exposure time. These factors also apply in two dimensional tracking studies. The typical resolution for x, y position determination here was 5 nm, which was greater than that of 1-2 nm in a previous report of two-dimensional SPT (Gelles et al, 1988). This difference in x,y resolution was due to

differences in signal-to-noise ratios and effective pixel size. It should be noted that the overall spatial resolution of our instrument was limited by the accuracy of z position determination to ≈ 12 nm at 600 nm wavelength. Further improvement in spatial resolution may be obtained by increasing the effective pixel size and/or signal intensity.

The maximum sampling rate for 3D tracking was determined by the acquisition and analysis of a particle image. The exposure and data transfer time for a 12 bit 40 x 40 pixel image was approximately 150 ms. The algorithms described in this study were implemented on a 25 MHz 486DX computer and required computation time of approximately 150 ms, giving a 3-4 Hz maximum sampling rate. To measure faster particle motions, the sampling rate could be increased by several approaches. Computation time could be reduced by using a faster computer. Images could be stored for post-experiment processing as reported in previous two dimensional SPT studies (De Brebander et al, 1989); however, a major disadvantage of image post-processing is that adjustment of the z position of the microscope stage cannot be accomplished during the experiment. Another approach would be to decrease the exposure time for image collection. However, in biological applications where particle fluorescence is low, brief exposure times may yield greater errors in position measurement.

Hysteresis and gear lash in the microscope fine focus control did not permit accurate determination of z position from the angular position of the motor. Because of this variability, many data points were required to generate calibration curves with high precision. This uncertainty associated with the mechanical movement of the stage also precluded high accuracy 3D SPT by continuous autofocussing control algorithms. Unlike an autofocussing method, our technique is capable of simultaneously tracking several particles by analysis of particle images.

The ability to track particles in three dimensions was demonstrated in artificial and biological systems. In artificial systems, the diffusion coefficient of particles in solutions of viscosities 30 and 56 cP solutions were in agreement with values predicted from the

Stokes-Einstein equation. Bead diffusion decreased in the presence of an immobile network, as theoretically predicted. 3D SPT was also applied to measure the diffusion of beads within cells. Analysis of the trajectory of these particles indicated confined diffusion. The ability to track shape changes in cells was demonstrated by the measurement of water permeability in individual adherent cells in culture. The strategy of tracking fluorescent beads at the cell surface could also be applied to study volume regulatory phenomena in individual cells, and to correlate volume regulation with intracellular ion activities. The 3D SPT method introduced here also has potential applications to a number of other biological problems including: a) the directed, diffusive and restricted motion of intracellular organelles, such as endocytic and secretory vesicles, providing information on the role of skeletal proteins and vesicular fusion in transport phenomena; b) the existence of immobile intracellular barriers to diffusive motions, such as the putative nuclear scaffold structure; and c) the direction of specific membrane components during cell motility and mitosis.

Chapter 4

CONSTRUCTION AND PERFORMANCE OF A FRAP INSTRUMENT WITH MICROSECOND TIME RESOLUTION

4.1 Summary

A FRAP apparatus to measure fluorescence recovery half-times down to 200 μs was constructed. Photobleaching pulses were formed using two acousto-optic modulators in series with a minimum pulse width of ≈ 6 μs. A photomultiplier and transimpedance amplifier were used to detect fluorescence signals which were digitized at rates of up to 1 MHz. A gating circuit was designed to protect the light detection system during the photobleaching pulse by switching the photocathode between the negative high voltage and first dynode voltage. Transient anode currents produced by capacitive coupling of the photocathode into the anode and other dynodes were subtracted from the measured signals to obtain the fluorescence recovery curves. The capacitive current transient affected the first 40 μs of the recovery curve. The recovery half-times of fluorescein dextrans (40-500 kD) in aqueous solution measured with this FRAP apparatus increased with dextran size as predicted by theory. To measure faster recoveries, modifications to the gating circuit are proposed to reduce the current transient amplitude and to further attenuate the photomultiplier response when gating circuit is activated.

4.2 Introduction

Fluorescence recovery after photobleaching (FRAP) is a well established method to measure the diffusive and directed mobilities of ensembles of fluorescent particles in

biological systems. Particle mobility is measured from the increase in fluorescence signal in a region after photobleaching by a brief, intense laser pulse. The time course of signal recovery is related to the mobility of the fluorescent particles and the measurement area or volume. In experiments where particle mobility is high or the measured region size is small, rapid recoveries are expected, with recovery half times of < 500 μs. For example, in total internal reflectance FRAP, a thin section (≈ 50 - 100 nm) at the surface of a sample is measured using the evanescent field laser beam undergoing total internal reflection at a dielectric interface. For measurements of particle mobility in cell organelles, the measured region size must be very small.

To measure rapid fluorescence recoveries after photobleaching, the FRAP apparatus must generate short, high intensity pulses (pulse widths < 100 μs) for photobleaching, protect the light detection system during this pulse from overload or damage, and record light intensity with microsecond time resolution immediately following this pulse. In this chapter, the construction and performance of a FRAP apparatus with microsecond time resolution is described.

4.3 Instrument Design

Optical Instrumentation

The intensity of a 350 mW 488 nm laser beam (Innova 70-2; Coherent, Palo Alto, CA) was modulated using 2 acousto-optic modulators (OD-8813 AOM with OD-8802 Modulator Driver; NEC, Sunnyvale, CA) in series (Fig. 4.1). The AOM drivers were modified to respond to 0-5 V analog voltages by removal of 74S04 Hex Inverter chip at the signal input and shorting the chip socket terminals 3 and 6. AOMs were positioned to diffract the incoming laser light maximally into the first order. 2 mm diameter pinholes were positioned 40 cm beyond the exit of each AOM to isolate the first order beams. The first order beam from the second AOM was directed into an epifluorescence microscope

Figure 4.1. Schematic of FRAP apparatus. Data acquisition was hardware triggered by the AOM control (connection not shown). See text for more details.

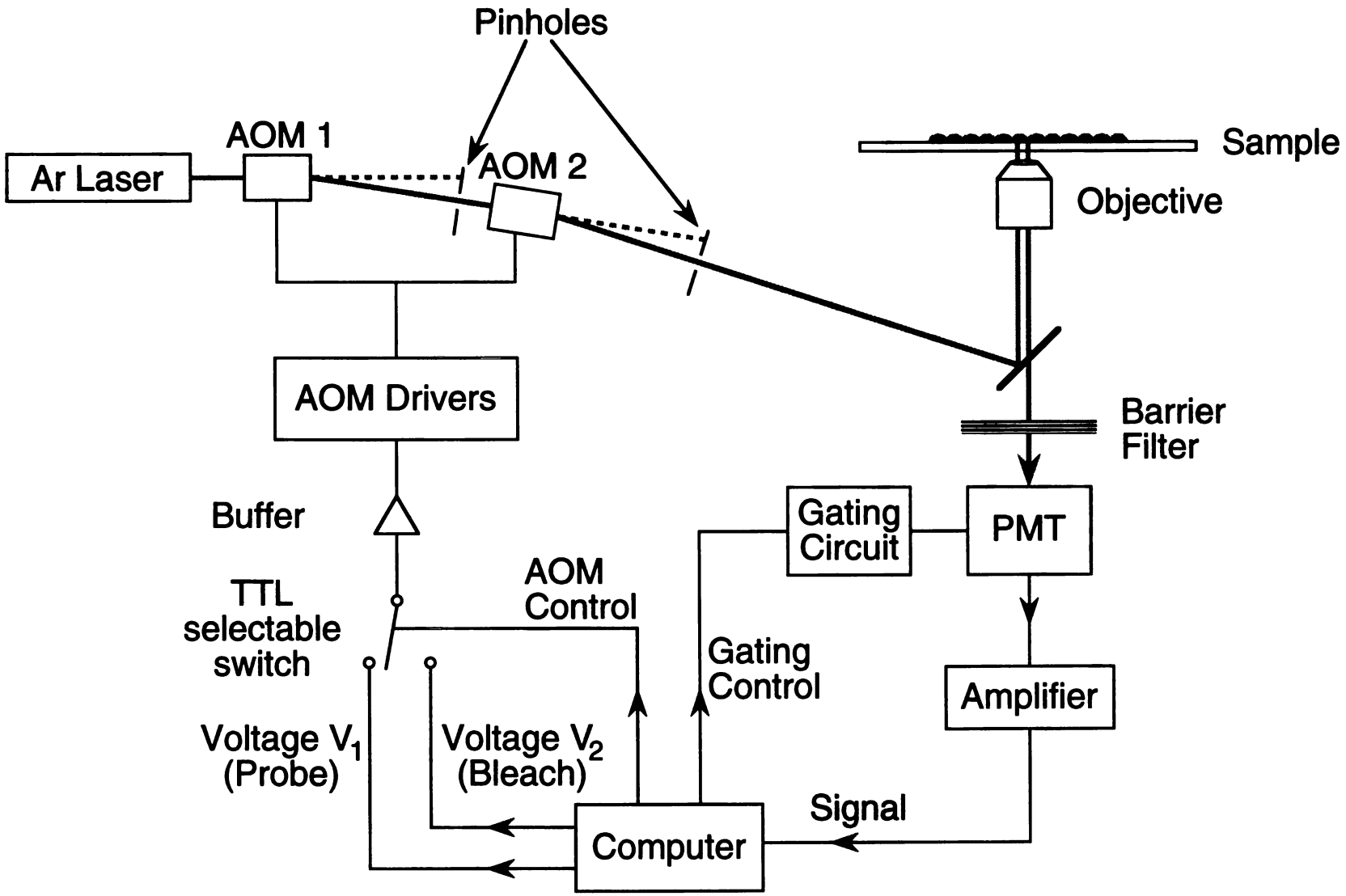
Pinholes
AOM 1
AOM 2
Ar Laser
Sample
Objective
AOM Drivers
Barrier
Filter
Buffer
Gating
Circuit
PMT
TTL
selectable
switch
AOM
Control
Gating
Control
Amplifier
Voltage V_1
(Probe)
Voltage V_2
(Bleach)
Signal
Computer

and focused onto the sample. Each AOM could modulate the intensity of the diffracted laser beam by a factor of > 10^3:1 so that beam intensity could be modulated over a range of > 10^6:1. During a typical FRAP experiment, the attenuation ratio (the ratio of the bleach beam intensity to the probe beam intensity) was adjusted to between 5,000 and 50,000.

Emitted fluorescence was collected through a 20 X objective (0.4 N.A.; Nikon), a 510 nm dichroic mirror, and GG515 barrier filter, and was detected using a photomultiplier (PMT) (9828A; Thorn EMI, Rockaway, NJ) operated at 500-900 V. The photomultiplier signal was amplified using a transimpedance amplifier with virtual ground input (A1; Thorn EMI, Rockaway, NJ) and gain conversion set to either 10^5 V/A (1 μs rise time) or 10^6 V/A (20 μs rise time). For slow fluorescence recovery times ($t_{1/2}$ > 10 ms), the amplifier was set to 10^6 V/A and the output was low-pass filtered (single pole, 350 Hz bandwidth) to increase signal-to-noise ratio.

Data Collection and Formation of Photobleaching Pulses

Amplified signals were digitized by a 12-bit analog-to-digital converter (Flash 12, Model 1; Strawberry Tree, Santa Clara, CA) at a sampling rate of up to 1 MHz. The fluorescence signal was measured over three time periods. Prior to the photobleaching pulse, the pre-bleach fluorescence signal was measured (typically 1,000-25,000 points sampled over 1 ms to 2.5 s). Following the photobleaching pulse, the recovery signal was measured (typically 5,000-100,000 points sampled over 5 ms to 10 s). After the recovery signal was collected, the final fluorescence signal was measured (15,000-20,000 points sampled over 4 s; points were acquired 25 ms to 40 s following the photobleaching pulse). These intervals were selected in reference to the period over which the pre-bleach signal was measured, T; the recovery signal was measured over 4 T, and the final recovery signal was collected after 20 T following the photobleaching pulse. For low light signals, 20-100 individual FRAP experiments were averaged to improve the signal

to noise ratio.

The intensities of the bleach and probe beams were set using the analog voltage outputs, V_1 and V_2, of the Flash 12 A/D board (Fig. 4.1). A high speed analog multiplexer (HI-518-5; Harris Semiconductor, Santa Clara, CA) was configured as an analog switch to select rapidly between the AOM voltages using a computer-generated TTL signal (AOM control, Fig. 4.1). The selected voltage was buffered using two AD811 high speed operational amplifiers (one per driver) configured as 50 Ω line drivers to supply the low impedance inputs of the AOM drivers. Data collection was hardware triggered to begin at the falling edge of AOM control signal.

This photomultiplier protection circuit required a second control signal (gating control, Fig. 4.1). To ensure that the photomultiplier was gated off during the photobleaching pulse, the gating control enabled the protection circuit at 2 μs before the start of the photobleaching pulse and disabled the circuit for 3 μs following the end of the pulse. Both the AOM control and gating control signals were generated using a precision microsecond timing board (PC-TIO-10; National Instruments, Austin, TX).

Photomultiplier Protection Circuit

For the duration of a photobleaching pulse, the photomultiplier was gated off by increasing the voltage at the photocathode of the photomultiplier from the negative high voltage supply to the first dynode voltage (Fig. 4.2). The circuit described here is a modification of the design of Yoshida et al. (1989). A driver circuit isolated and transformed the computer-generated TTL gating signal into a signal to switch the photocathode voltage. In the driver, the control signal from the computer was isolated using a 6N137 high speed optocoupler (maximum rated isolation = 2500 V RMS). The driver circuitry was powered by a 17 V dc power supply referenced to 9.1 V below the photocathode voltage. The signal from the optocoupler was amplified by an AD811 high speed operational amplifier configured with a gain of 2.75. The driver circuit was biased

Figure 4.2. Photomultiplier protection circuit. Diodes provided 4.5 V to the 6N137 optoisolator. 9.1 V Zener diode referenced the driver circuit to 9.1 V below the photocathode voltage. See text for more details.

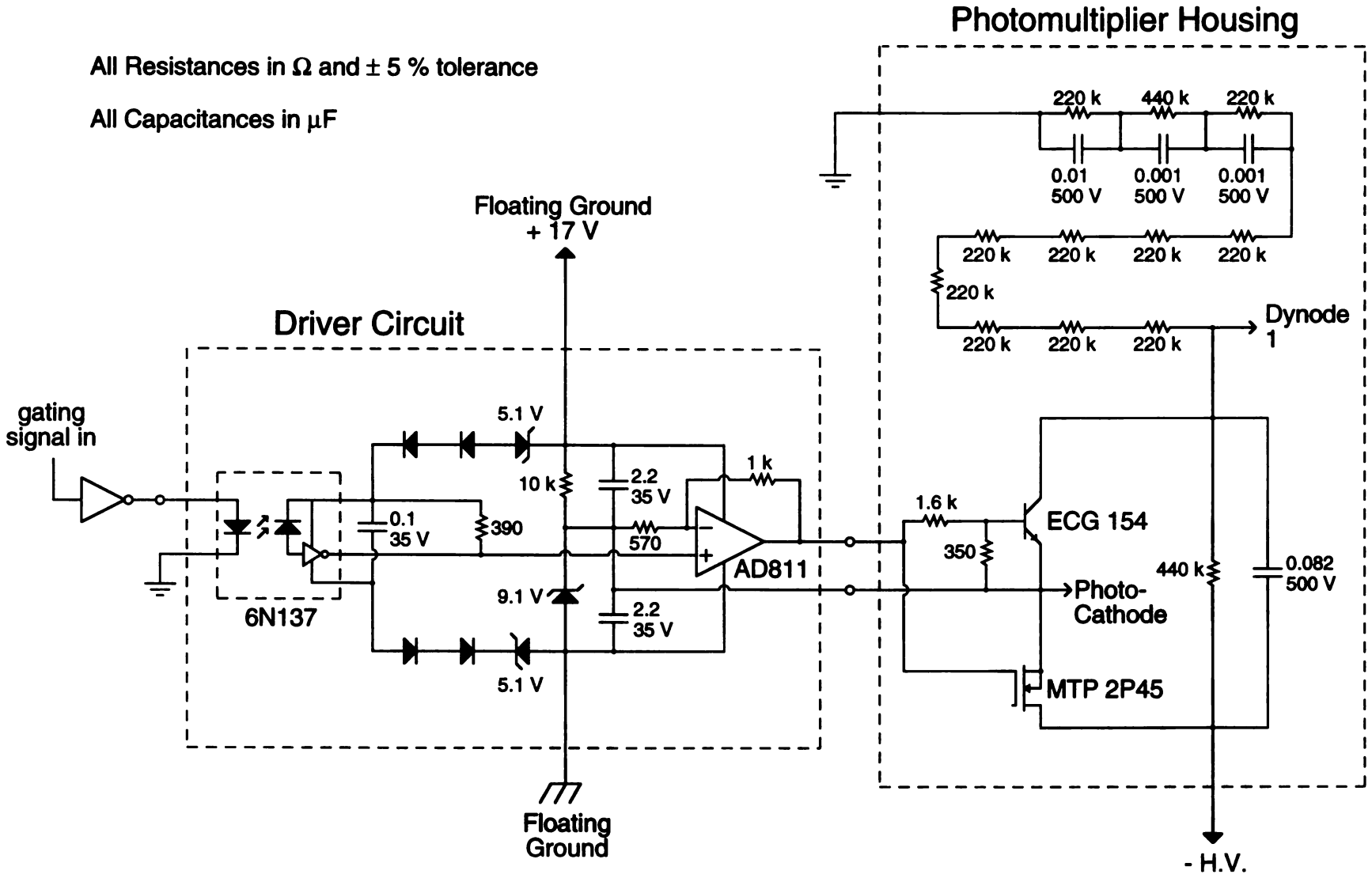
All Resistances in Ω and ± 5 % tolerance
All Capacitances in μF
Photomultiplier Housing
220 k
440 k
220 k
0.01
500 V
0.001
500 V
0.001
500 V
220 k
220 k
220 k
220 k
220 k
Dynode
1
220 k
220 k
220 k
220 k
Floating Ground
+ 17 V
Driver Circuit
gating
signal in
5.1 V
10 k
2.2
35 V
1 k
0.1
35 V
390
570
AD811
1.6 k
ECG 154
350
440 k
0.082
500 V
Photo-
Cathode
9.1 V
2.2
35 V
6N137
MTP 2P45
5.1 V
Floating
Ground
- H.V.

so that signals from the AD811 were either 6 V below (gating signal low) or 4.8 V above (gating signal high) the photocathode voltage.

The photocathode voltage could be set to the first dynode or the negative voltage supply using power transistors. A high voltage NPN power transistor (ECG 154) was connected between the cathode and first dynode, and a P channel MOSFET transistor (MTP 2P45) was connected between the cathode and negative high voltage supply. When the driver signal was high (4.8 V above the photocathode voltage), the NPN transistor was on while the MOSFET was off and the photocathode was held at the first dynode voltage. When the signal was close to that of the photocathode voltage, both transistors were off and the photocathode was cut off from both the first dynode and the negative high voltage. When the signal was low (6 V below the photocathode voltage), the MOSFET was on while the NPN transistor was off so that the photocathode was held at the negative high voltage value.

Large transients in the anode current were generated during photomultiplier gating by capacitive coupling of the photocathode into the anode and other dynodes (see below). The transient signal, x(t), over the recovery period was recorded using a non-fluorescent sample prior to each experiment. Over the recovery period, the fluorescence signal, s(t), was obtained by subtracting this transient signal from the measured signal, m(t), ($s(t) = m(t) - x(t)$; $0 < t < 4$ T). Over the pre-bleach and final periods, s(t) was obtained by subtracting the dark current measured using the non-fluorescent sample, I_d ($s(t) = m(t) - I_d$; $-T < t < 0$ and $t > 20$ T). Typically, 25 transient curves were averaged and 10,000 points were averaged to obtain the dark current.

4.4 Instrument Performance

A transient artifact was produced when the photomultiplier was gated. The transient current at the anode appeared to have two distinct transient components: a set of

high amplitude current pulses (≈ 1000 μA) during the first 2 μs after switching followed by a low amplitude (≈ 2 μA) exponential decay with time constant ≈ 12 μs (anode current, Fig. 4.3 A). The initial high amplitude transient was not caused by a short circuit of the first dynode to the negative high voltage supply during gating because no large transients are observed in the photocathode voltage or the first dynode voltage during a gating pulse (photocathode voltage, first dynode voltage, Fig. 4.3 A). The low amplitude transient was not an overload response of the amplifier because the amplifier was not overloaded by the large amplitude transient. These transient components in the anode current probably were caused by capacitive coupling of the cathode voltage to the anode and the dynodes - the initial, high amplitude component corresponded to the capacitive current from the cathode into the anode, and the low amplitude component corresponded to the capacitive current through the dynodes. The time constant of the low amplitude component was determined by resistance of the voltage divider circuit and capacitances associated with each dynode. At higher amplifier gains and lower bandwidths, the shape and duration of these current transients changed. At a gain of 10^5 V/A (1 μs rise time), the transient was similar in shape but reduced in amplitude (top, Fig. 4.3 B). At a gain of 10^5 V/A and smaller bandwidths, the amplitude of the transients decreased and their duration increased (middle and bottom, Fig. 4.3 B)

The gating transients were consistent in amplitude and duration from pulse to pulse. The transients were independent of illumination and could be subtracted from an actual waveform to obtain the measured light signal (Fig. 4.4 A, B). At amplifier settings of 10^5 and 10^6 V/A, the measured signal returned to within ≈ 5 % of its pre-gating level by ≈ 40 μs after the gating pulse. During this first 40 μs and in the off state, the corrected signal was still affected by the gating transient. Transients were also observed in corrected signals in the absence of illumination and the transient amplitude increased when the number of averaged curves was decreased (data not shown). The transients in the corrected signals were probably caused by timing jitter between the transient and

Figure 4.3. Transient current response during photomultiplier gating. A. Anode current, photocathode voltage, and first dynode voltage measured during a photomultiplier gating pulse of 70 μs. Anode current was measured with amplifier gain at 1000 V/A and 20 ns rise time. Photomultiplier voltage was set at -450 V. **B.** Anode current measured at the specified amplifier gains and corresponding rise times during a gating pulse (gating pulses not shown). The width of the gating pulses for each curve were selected to display the entire transient associated with gating the photomultiplier off. Photomultiplier voltage was set at -800 V. All curves were recorded using a Tektronix 2201 digital oscilloscope.

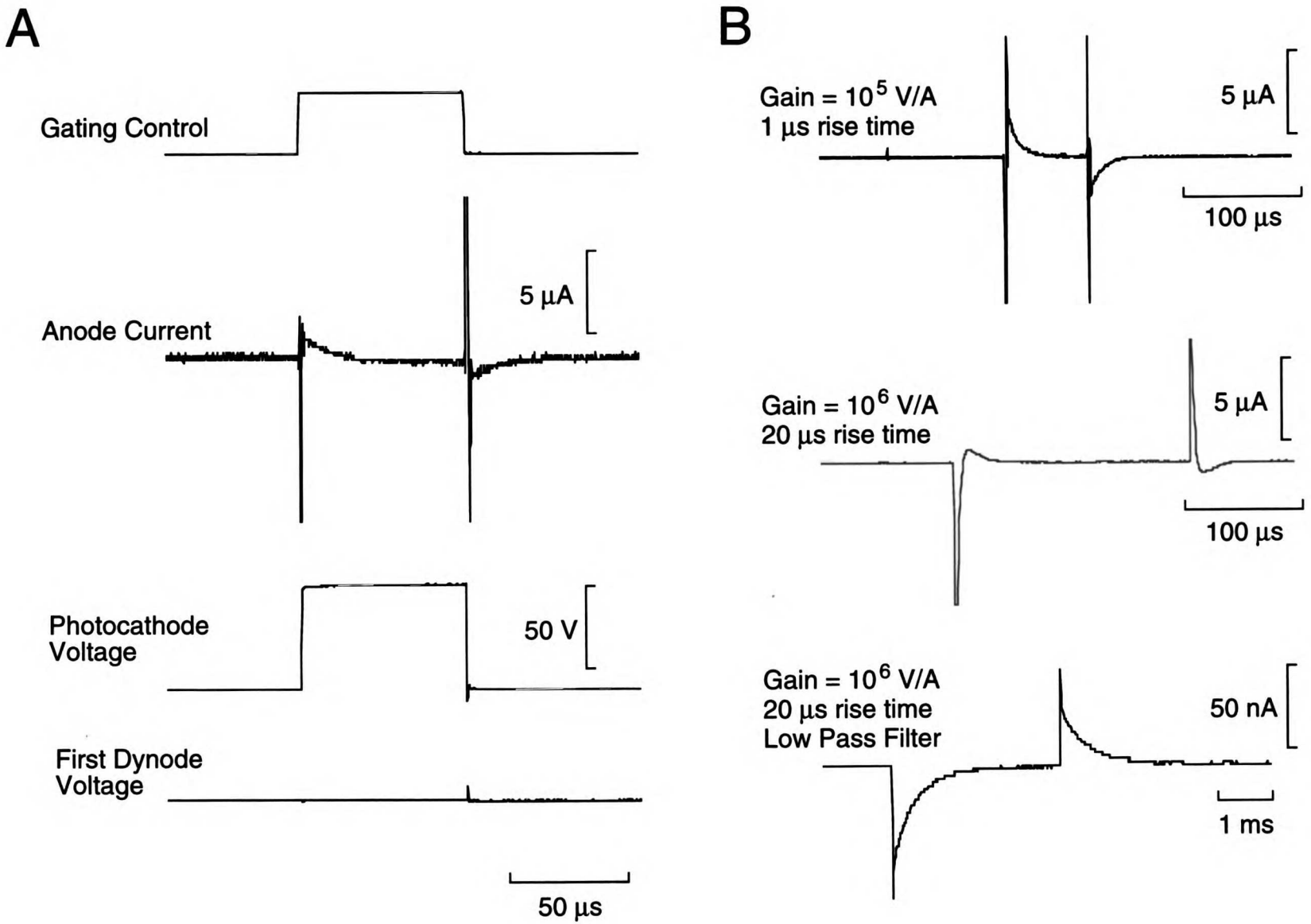
A
Gating Control
5 µA
Anode Current
Photocathode
Voltage
50 V
First Dynode
Voltage
50 µs
B
Gain = 10^5 V/A
1 µs rise time
5 µA
100 µs
Gain = 10^6 V/A
20 µs rise time
5 µA
100 µs
Gain = 10^6 V/A
20 µs rise time
Low Pass Filter
50 nA
1 ms

Figure 4.4. Subtraction of the current transient from the measured waveforms. Under constant illumination, the photomultiplier current was measured during a gating pulse. The gating transient measured was subtracted from each measured waveform to obtain the corrected light signal at amplifier gain conversions of **A.** 10^5 V/A, and **B.** 10^6 V/A. All curves were the averaged 25 times and were measured using the FRAP apparatus described in the text.

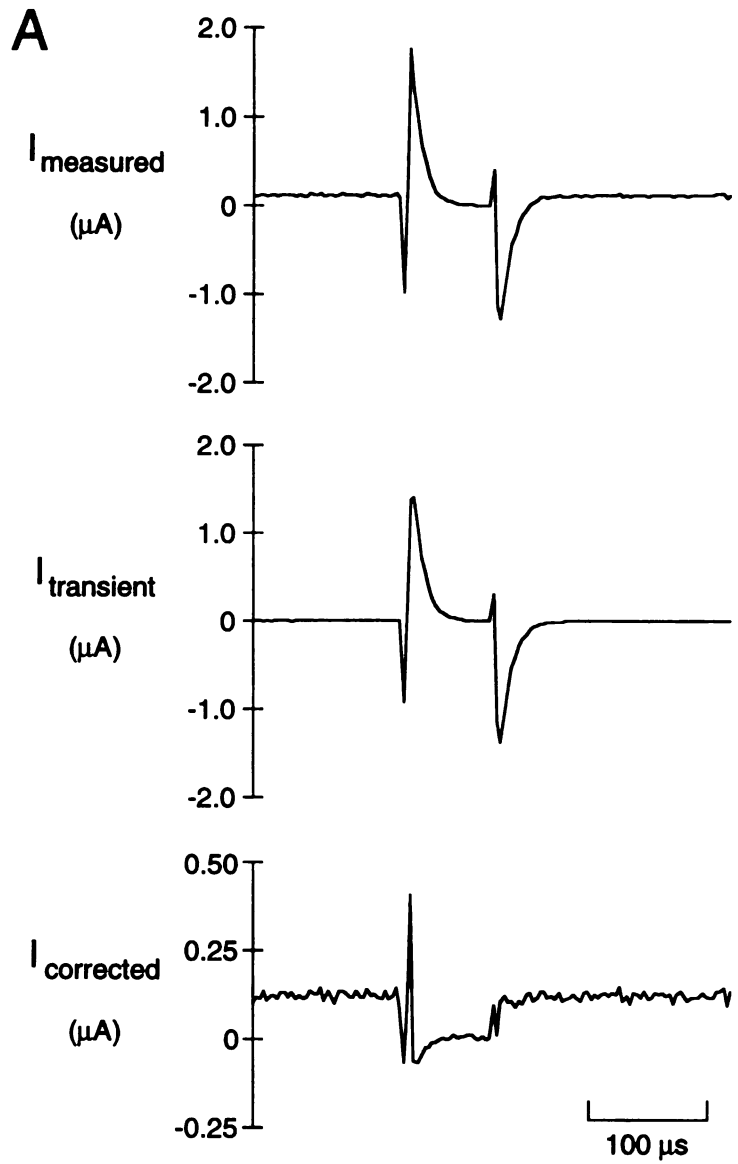
A
I measured (μA)
2.0
1.0
0
-1.0
-2.0
I transient (μA)
2.0
1.0
0
-1.0
-2.0
I corrected (μA)
0.50
0.25
0
-0.25
100 μs

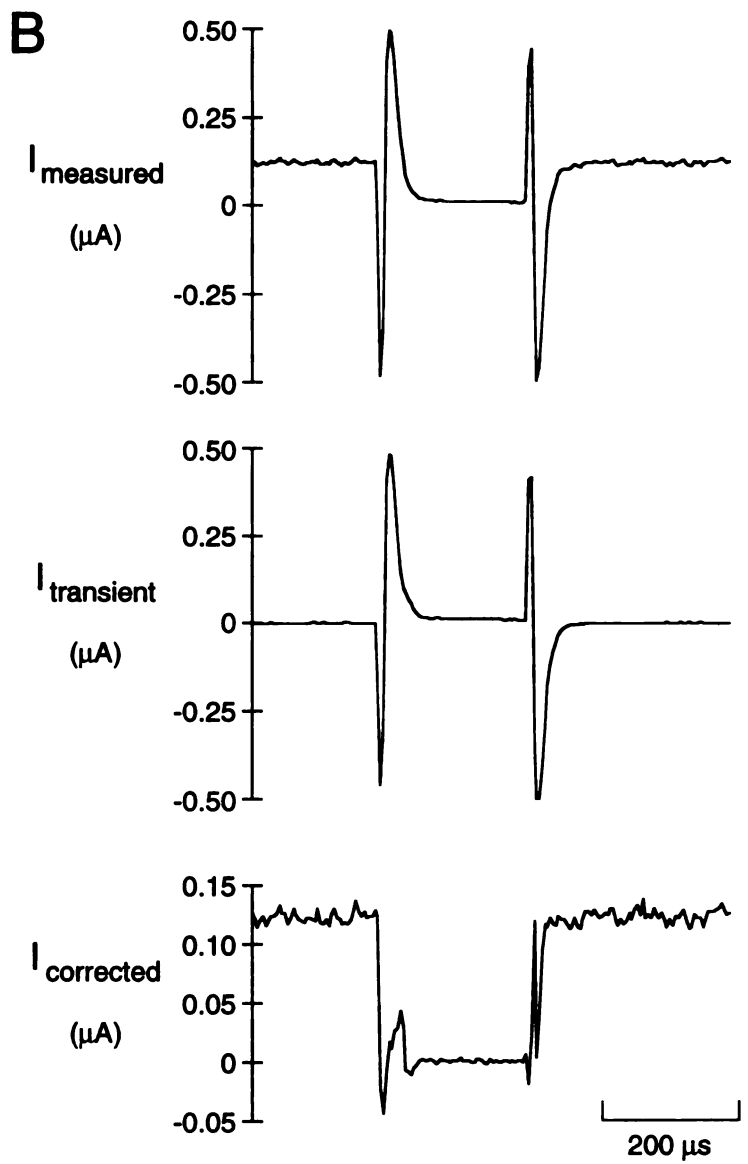
B
I measured (μA)
0.50
0.25
0
-0.25
-0.50
I transient (μA)
0.50
0.25
0
-0.25
-0.50
I corrected (μA)
0.15
0.10
0.05
0
-0.05
200 μs

measured current waveforms. The triggering circuitry on the A/D board could begin data acquisition only within 1 sampling period of receiving the trigger signal from the AOM control (for the Strawberry Tree A/D Flash 12 board, the sampling period was set to either 1, 4 or 16 μs, depending upon the data sampling rate); hence there was up to 1 sampling period timing uncertainty associated with collecting each curve. Timing difference between the transient and the measured currents could cause the appearance of the transient in the corrected waveform. If the duration of the transients was increased, such as with low pass filtering of the amplifier output, the observed signal was within 5 % of its pre-gating level approximately at 1.5 ms following the bleaching pulse with no appearance of the gating transient (data not shown).

The minimum half time measurable with this FRAP apparatus is limited by the presence of the artifactual transient signal in the corrected signal. Without the low pass filter, the first 40 μs of data is unusable because of the transients. If this initial 40 μs of data is assumed to be 20 % of the minimum measurable recovery half time, then this apparatus can measure half times down to 200 μs. The timing specifications of this gating circuit with this photomultiplier can be estimated from the switching of the photocathode voltage because timing jitter does not permit accurate timing measurements using the photomultiplier signal (photocathode voltage, Fig. 4.3 A). The 10-90 % on and off times were 200 ns and 600 ns, respectively. The on and off delay times (the time from the beginning of the gating control signal to when the photocathode voltage has changed by 10 % of the total voltage swing) were 800 and 500 ns, respectively.

The formation of brief laser pulses could be achieved with μs accuracy (Fig. 4.5 A). The on and off times (10-90 %) of a light pulse were ≈ 3.5 and 1.8 μs, respectively. These rise times limit the minimum pulse width to ≈ 6 μs. During the high intensity light pulse, the PMT signal is determined by the extinction ratio of the gating circuit (the ratio of the PMT current in the on and gated off states), which for this system was measured to be 480:1. The ability of the gating circuit to block high intensity light was tested by

Figure 4.5. Formation of photobleaching light pulses and protection of the light detection system. **A.** The laser intensity during a 70 μs photobleaching pulse was measured while the photomultiplier protection circuit was disabled. **B.** The laser intensity was measured during a 220 μs photobleaching pulse while the protection circuit was enabled. The attenuation ratio was set to ≈ 10,000.

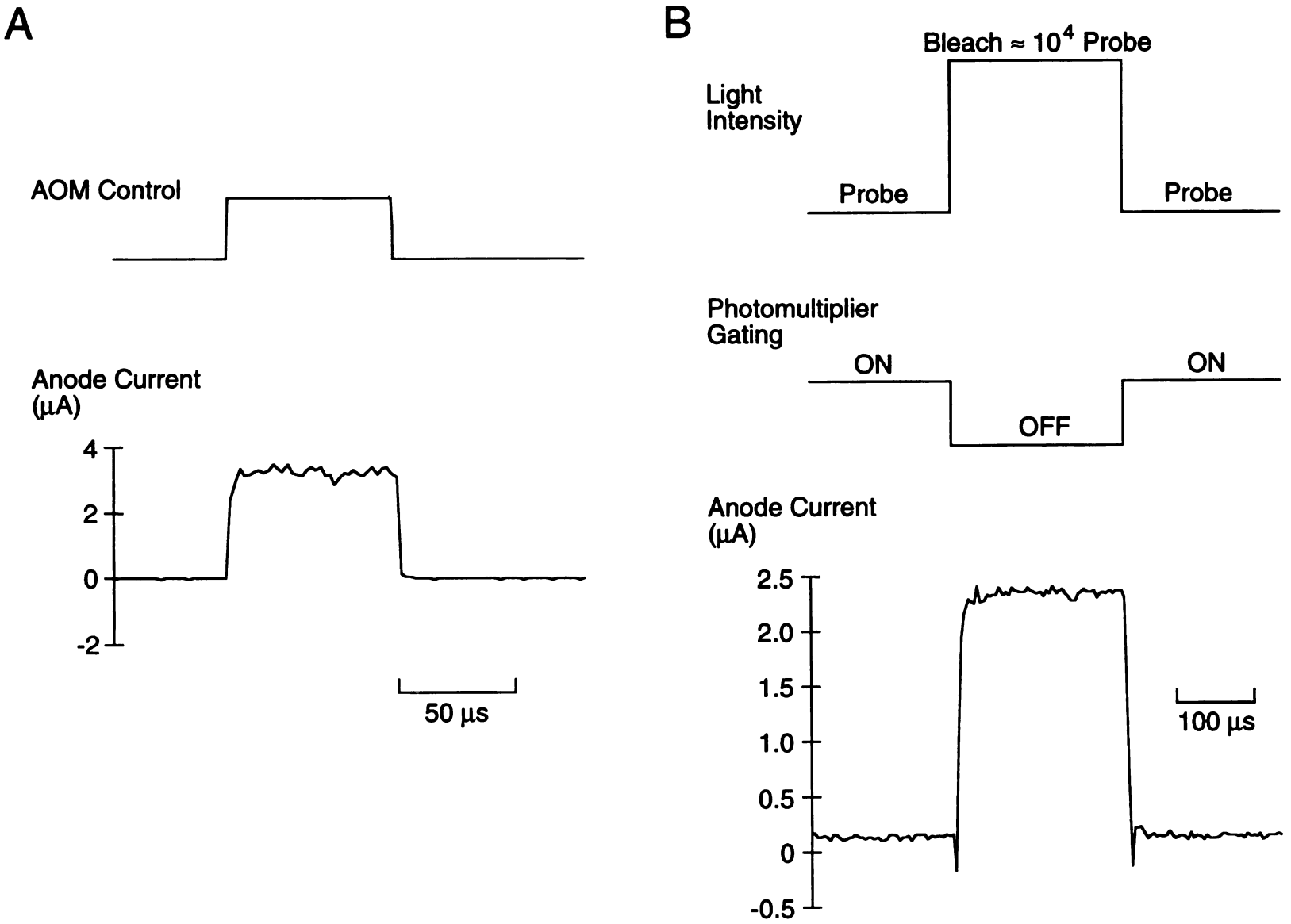
A
AOM Control
Anode Current
(μA)
4
2
0
-2
50 μs
B
Bleach ≈ 10^4 Probe
Light
Intensity
Probe
Probe
Photomultiplier
Gating
ON
OFF
ON
Anode Current
(μA)
2.5
2.0
1.5
1.0
0.5
0
-0.5
100 μs

measuring the probe and bleach beams at typical experiment settings (probe signal ≈ 100 nA, probe-to-bleach intensity ratio ≈ 10^4). During a photobleaching pulse, a large signal was observed in the off state (Fig. 4.5 B). This signal was ≈ 20 x higher than the probe beam signal, as expected, because the extinction ratio of the gating circuit decreased the bleach beam signal by ≈ 500.

The diffusional mobility of fluorescein dextrans in dilute aqueous solution was measured with this FRAP apparatus (Fig. 4.6). The half times for recovery are theoretically expected to scale proportionally to the radii of rigid, spherical molecules. For 40 kD, 150 kD and 500 kD dextrans, the measured times were 84 ms, 230 ms and 260 ms, which scaled approximately in proportion to the predicted radii of 27, 42 and 63, respectively (Luby-Phelps et al., 1986). Differences of the proportionality of the half times are attributable to the non-spherical shape of the dextran molecules.

4.5 Discussion

The FRAP apparatus described in this chapter was capable of measuring fluorescence recoveries down to 200 μs. Faster recoveries could be measured by reducing the amplitude and duration of the transients associated with the PMT gating circuit which affected the initial data points collected by the apparatus. These transients are unavoidable for any gating technique which swings the voltage across a dynode or set of dynodes because of capacitive coupling into the anode and other dynodes. However, transient amplitude can be reduced by swinging the voltage at a point with small capacitive coupling to the other dynodes and the anode. The photocathode, because of its large surface area, has a large capacitance to the other dynodes. The first dynode, however, has a smaller surface area and smaller capacitance to the other dynodes and would be more suitable for PMT gating. Alternatively, a PMT with a focus or gating electrode could be used. Such an electrode, which is located between the first dynode

Figure 4.6. Measurement of the diffusion of fluorescein dextrans in water. Fluorescence recovery curves are shown for 40 kD, 150 kD and 500 kD dextrans in 1 % w/w aqueous solution. For each curve, the bleach beam was adjusted to give ≈ 30 % bleaching. Each curve is the average of 10 recovery curves. The final portion of the curve following the double slashes (//) represent the fluorescence signals measured at 50 $t_{1/2}$.

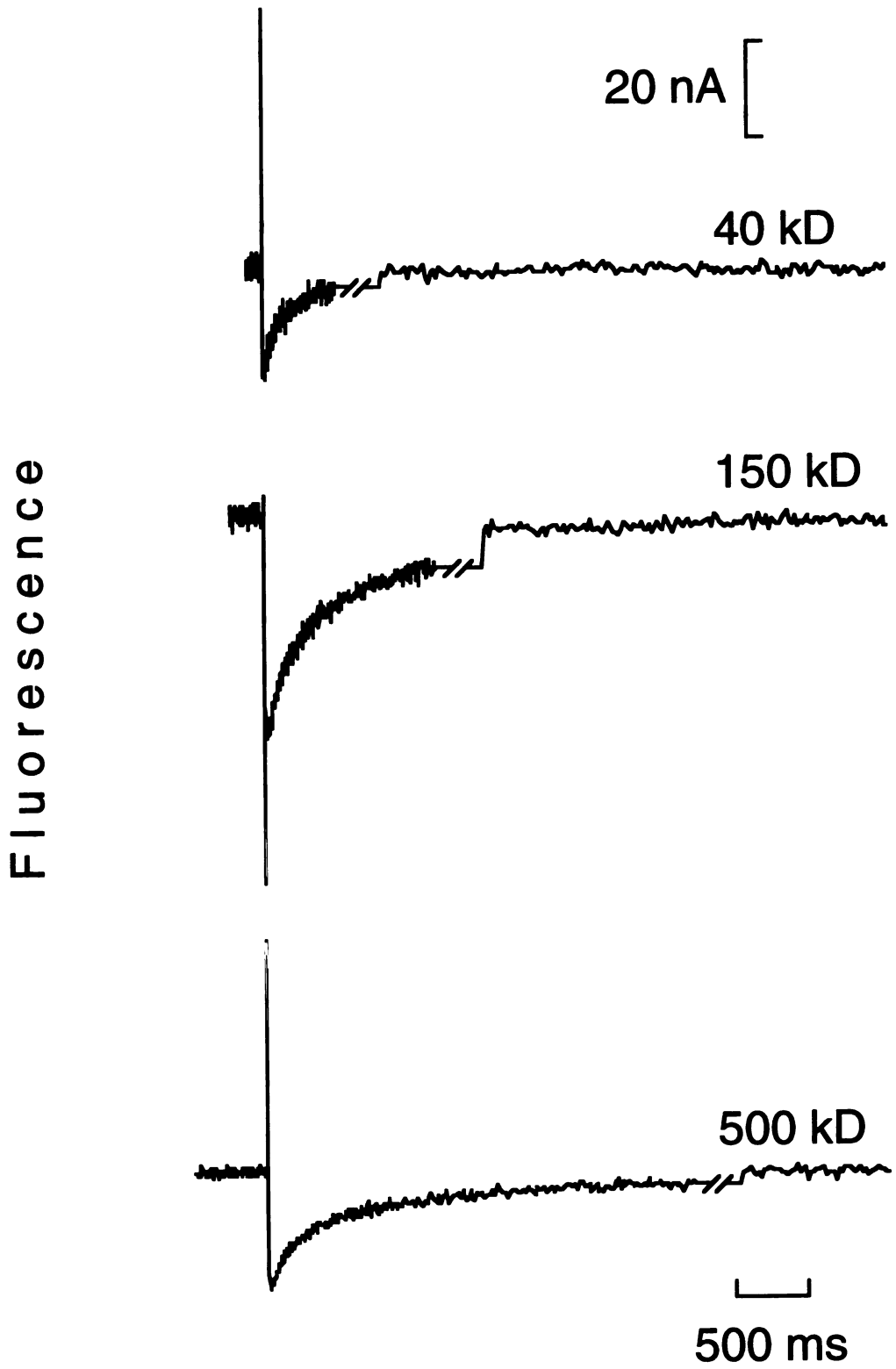
20 nA
40 kD
150 kD
500 kD
Fluorescence
500 ms

and photocathode, can be used to gate the photomultiplier off while keeping transient currents small because of its inherently small inter-dynode capacitances.

Another factor affecting the measurement of fast recoveries with this FRAP apparatus is the extinction ratio of the gating circuit. As the recovery half time decreases, the photobleaching pulse width must correspondingly decrease. To photobleach the same percentage of the fluorescent molecules within the measured region with a shorter photobleaching pulse, the intensity of the photobleaching pulse must increase. For very rapid recoveries, the extinction ratio of the circuit may not be sufficient to prevent the PMT from exceeding its maximum current rating during the photobleaching pulse. To increase the extinction ratio, the first dynode voltage should be more negative than the photocathode during the photobleaching pulse in order to repel photoelectrons. To achieve this, the photocathode could be switched up to the second dynode voltage (Fig. 4.7 A). Alternately, the first dynode or a gating electrode could be switched down to a voltage below the photocathode created by adding one resistor to the resistive ladder network of the photomultiplier (Fig. 4.7 B). However, a drawback of this approach is that larger current transients will be created because larger voltage swings will be required.

Figure 4.7. Alternate gating circuit configurations to increase extinction ratio. A. Configuration where the photomultiplier is gated off by switching the photocathode voltage up to the second dynode voltage. **B.** Configuration where the photomultiplier is gated off by switching the first dynode down below the photocathode voltage.

A

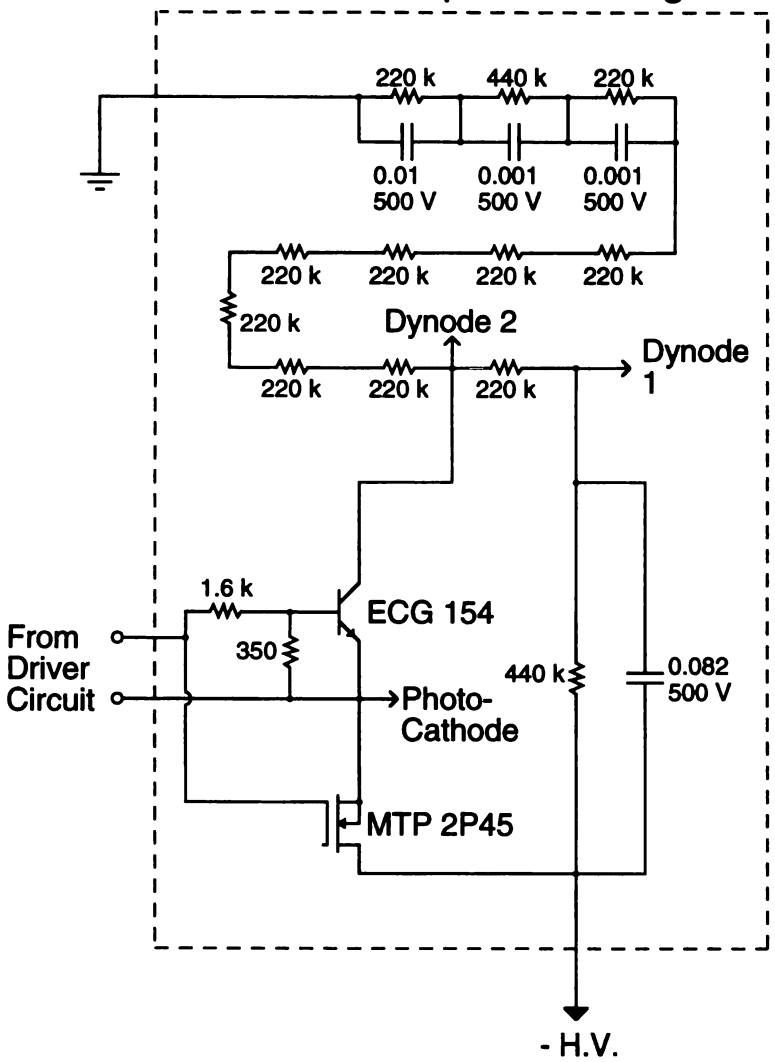
Photomultiplier Housing
220 k
440 k
220 k
0.01
500 V
0.001
500 V
0.001
500 V
220 k
220 k
220 k
220 k
220 k
Dynode 2
Dynode
1
220 k
220 k
220 k
1.6 k
ECG 154
From
Driver
Circuit
350
Photo-
Cathode
440 k
0.082
500 V
MTP 2P45
- H.V.

B

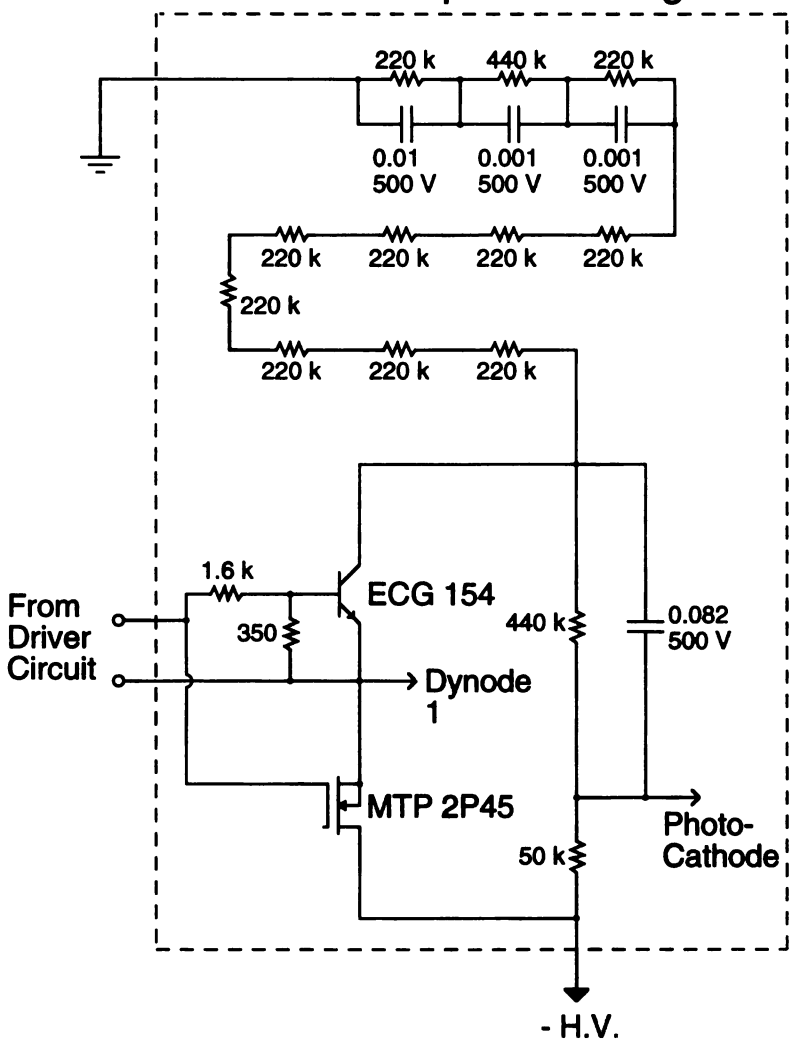
Photomultiplier Housing
220 k
440 k
220 k
0.01
500 V
0.001
500 V
0.001
500 V
220 k
220 k
220 k
220 k
220 k
220 k
220 k
220 k
1.6 k
ECG 154
From
Driver
Circuit
350
Dynode
1
440 k
0.082
500 V
MTP 2P45
Photo-
Cathode
50 k
- H.V.

BIBLIOGRAPHY

Axelrod, D., D. E. Koppel, J. S. Schlessinger, E. Elson, and W. W. Webb. 1976. Mobility measurement by analysis of fluorescence photobleaching recovery kinetics. *Biophys. J.* 16:1055-1069.

Barisas, B. G. 1980. Criticality of beam alignment in fluorescence photobleaching recovery experiments. *Biophys. J.* 29:545-548.

Bertch, M. A., and D. E. Koppel. 1988. Fluorescence redistribution after photobleaching -- the effect of diffusion during bleaching. *Biophys. J.* 53:512a (Abstract).

Bjarneson, D. W., and N. O. Petersen. 1991. Effects of second order photobleaching on recovered diffusion parameters from fluorescence photobleaching recovery. *Biophys. J.* 60:1128-1131.

Blackwell, M. F., and J. Whitmarsh. 1990. Effect of integral membrane proteins on the lateral mobility of plastoquinone in phosphatidylcholine proteoliposomes. *Biophys. J.* 58:1259-1271.

Blatter, L. A., and W. G. Wier. 1990. Intracellular diffusion, binding, and compartmentalization of the fluorescent calcium indicators indo-1 and fura-2. *Biophys. J.* 58:1491-1499.

Blum, F. D., S. Pickup, and K. R. Foster. 1986. Solvent self-diffusion in polymer solutions. *J. Colloid Interface Sci.* 113:336-341.

Bridgman, P. C., and T. S. Reese. 1984. The structure of cytoplasm in directly frozen cultured cells. I. Filamentous meshworks and the cytoplasmic ground substance. *J. Cell Biol.* 99:1655-1668.

Calaut, T. M., J. A. Dix, and A. S. Verkman. 1989. Fluorescence depolarization of cis- and trans-parinaric acids in artificial and red cell membranes resolved by a double hindered rotational model. *Biochemistry.* 28:5051-5058.

Chao, A. C., J. A. Dix, M. Sellers, and A. S. Verkman. 1989. Fluorescence measurement of chloride transport in monolayer cultured cells: mechanisms of chloride transport in fibroblasts. *Biophys. J.* 56:1070-1081.

Clegg, J. S. 1984. Intracellular water and the cytomatrix: some methods of study and current views. *J. Cell Biol.* 99(1, Pt. 2):167s-171s.

Couch, L. W. 1987. *Digital and Analog Communication Systems.* Macmillan Pub. Co., New York. 430-431.

De Brebander, M., H. Geerts, R. Nuydens and R. Nuyens. 1989. Detection of gold probes with video-enhanced contrast microscopy: Nanovid microscopy. *Am. J. Anat.* 185:282-295.

Dix, J. A., and A. S. Verkman. 1990. Mapping of fluorescence anisotropy in living cells by ratio imaging: application to cytoplasmic viscosity. *Biophys. J.* 57:231-240.

Drake, R. D., and J. Klafter. 1990. Dynamics of confined molecular systems. *Phys. Today.* 43(5):46-55.

Elson, E. L., and H. Qian. 1989. Interpretation of fluorescence correlation spectroscopy and photobleaching recovery in terms of molecular interactions. *Methods Cell Biol.* 30:307-332.

Elson, E. L., and J. A. Reidler. 1979. Analysis of cell surface interactions by measurements of lateral mobility. *J. Supramol. Struct.* 12:481-489.

Fujita, H. 1961. Free-volume model of diffusion in polymer solutions. *Adv. Polymer Sci.* 3:1-47.

Fulton, A. B. 1982. How crowded is the cytoplasm? *Cell.* 30:345-347.

Furukawa, R., J. L. Arauz-Lara, and B. R. Ware. 1991. Self-diffusion and probe diffusion in dilute and semidulute aqueous solutions of dextran. *Macromolecules.* 24:599-605.

Fushimi, K., and A. S. Verkman. 1991. Low viscosity in the aqueous domain of cell cytoplasm measured by picosecond polarization microscopy. *J. Cell Biol.* 112:719-725.

Fushimi, K., J. A. Dix, and A. S. Verkman. 1990. Cell membrane fluidity in the intact kidney proximal tubule measured by orientation-independent fluorescence anisotropy imaging. *Biophys. J.* 57:241-254.

Geerts, H., M. De Brebander, R. Nuydens, S. Geuens, M. Moeremans, J. De May and P. Hollenbeck. 1987. Nanovid tracking: A new automatic method for the study of mobility in living cells based on colloidal gold and video microscopy. *Biophys. J.* 52:775-782.

Gelles, J., B. J. Schnapp, M. P. Sheetz. 1988. Tracking kinesin-driven movements with nanometer-scale precision. *Nature.* 331: 450-453.

Gershon, N. D., K. R. Porter, and B. L. Trus. 1985. The cytoplasmic matrix: its volume and surface area and the diffusion of molecules through it. *Proc. Natl. Acad. Sci. USA.* 82:5030-5034.

Gibson, S. F. and F. Lanni. 1991. Experimental test of an analytical model of aberration in an oil-immersion objective lens used in three dimensional light microscopy. *J. Opt. Soc. Am. A.* 8: 1601-1613.

Gonzalez, R. C. and P. Wintz. 1987. *Digital Image Processing*. Second Edition. Addison-Wesley Pub. Co., Reading. 334-340.

Gross, D. J. and W. W. Webb. 1988. Cell surface clustering and mobility of the liganded LDL receptor measured by digital video fluorescence microscopy. *In* Spectroscopic Membrane Probes, Vol. II. L. M. Loew, ed. CRC Press, Inc., Boca Raton. 19-47.

Hiraoka, Y., J. W. Sedat and D. A. Agard. 1990. Determination of the three-dimensional imaging properties of a light microscope system: Partial confocal behavior in epifluorescence microscopy. *Biophys. J.* 57: 325-333.

Hou, L., F. Lanni, and K. Luby-Phelps. 1990. Tracer diffusion in F-actin and ficoll mixtures: toward a model for cytoplasm. *Biophys. J.* 58:31-43.

Inoué, S. 1986. *Video Microscopy*. Plenum Pub., New York. 334-338.

Jacobson, K., A. Ishihara, and R. Inman. 1987. Lateral diffusion of proteins in membranes. *Ann. Rev. Physiol.* 49:163-175.

Jacobson, K., and J. Wojcieszyn. 1984. The translational mobility of substances within the cytoplasmic matrix. *Proc. Natl. Acad. Sci.* 81:6747-6751.

Jähnig, F. 1981. No need for a new membrane model. *Nature (London).* 289:694-696.

James, M. L., G. M. Smith, J. C. Wolford. 1985. *Applied Numerical Methods for Digital Computation*. Third Edition. Harper & Row Pub., New York. 396-397.

Keith, A. D., W. Snipes, R. J. Mehlhorn, and T. Gunter. 1977. Factors restricting diffusion of water-soluble spin labels. *Biophys. J.* 19:205-218.

Keith, A. D. 1973. Viscosity of cellular protoplasm. *Science (Wash. DC).* 183:666-668.

Koppel, D. E. 1981. Association dynamics and lateral transport in biological membranes. *J. Supramol. Struct. Cell. Biochem.* 17:61-67.

Kreis, T. E., B. Geiger, and J. Schlessinger. 1982. Mobility of microinjected rhodamine actin within living chicken gizzard determined by fluorescence photobleaching recovery. *Cell.* 29:835-845.

Landry, M. R., Q-j. Gu, and H. Yu. 1988. Probe molecule diffusion in polymer solutions. *Macromolecules.* 21:1158-1165.

Lee, G., A. Ishihara and K. A. Jacobson. 1991. Direct observation of brownian motion of lipids in a membrane. *Proc. Natl. Acad. Sci. USA.* 88:6274-6278.

Lepock, J. R., K. H. Cheng, S. D. Campbell, and J. Kruuv. 1983. Rotational diffusion of tempone in the cytoplasm of chinese hamster lung cells. *Biophys. J.* 44:405-412.

Lindmo, T., and H. B. Steen. 1977. Flow cytometric measurement of the polarization of fluorescence from intracellular fluorescein in mammalian cells. *Biophys. J.* 18:173-187.

Luby-Phelps, K., and D. L. Taylor. 1988. Subcellular compartmentalization by local differentiation of cytoplasmic structure. *Cell Motil.* 10:28-37.

Luby-Phelps, K., F. Lanni, and D. L. Taylor. 1988. The submicroscopic properties of cytoplasm as a determinant of cellular function. *Ann. Rev. Biophys. Biophys. Chem.* 17:369-396.

Luby-Phelps, K., P. E. Castle, D. L. Taylor, and F. Lanni. 1987. Hindered diffusion of inert tracer particles in the cytoplasm of mouse 3T3 fibroblasts. *Proc. Natl. Acad. Sci. USA.* 84:4910-4913.

Luby-Phelps, K., D. L. Taylor, and F. Lanni. 1986. Probing the structure of cytoplasm. *J. Cell Biol.* 102:2015-2022.

Ma, T., A. Frigeri, S.-H. Tsai, J. M. Verbavatz and A. S. Verkman. Localization and functional analysis of CHIP28k water channels in stably transfected chinese hamster ovary cells. *J. Biol. Chem.* 268: 22756-22764.

Mastro, A. M., and A. D. Keith. 1984. Diffusion in the aqueous compartment. *J. Cell Biol.* 99(1, Pt. 2):180s-187s.

Mastro, A. M., M. A. Babich, W. D. Taylor, and A. D. Keith. 1984. Diffusion of a small molecule in the cytoplasm of mammalian cells. *Proc. Natl. Acad. Sci. USA.* 81:3414-3418.

Miner, C. S. and N. N. Dalton. 1953. *Glycerol.* Reinhold Pub. Corp. New York. 279-322.

Periasamy, N., H. P. Kao, K. Fushimi, and A. S. Verkman. 1992. Organic osmolytes increase cytoplasmic microviscosity in kidney cells. *Am. J. Physiol.* 263: C901-907.

Phillies, G. D. J. 1989. The hydrodynamic scaling model for polymer self-diffusion. *J. Phys. Chem.* 93:5029-5039.

Porter, K. R. 1984. The cytomatrix: a short history of its study. *J. Cell Biol.* 99(1, Pt. 2):3s-12s.

Pusey, P. N., and R. J. A. Tough. 1985. Particle interactions. *In* Dynamic Light Scattering: Applications of Photon Correlation Spectroscopy. R. Pecora, editor. Plenum Publishing Corp., New York. 85-179.

Qian, H., M. P. Sheetz and E. L. Elson. 1991. Single particle tracking: analysis of diffusion and flow in two-dimensional systems. *Biophys. J.* 60: 910-921.

Salmeen, I., P. Zacmanidis, G. Jesion and L. A. Feldkamp. 1985. Motion of mitochondria in cultured cells quantified by analysis of digitized images. *Biophys. J.* 48: 681-686.

Saxton, M. J. 1989. Lateral diffusion in an archipelago: distance dependence of the diffusion coefficient. *Biophys. J.* 56: 615-622.

Saxton, M. J. 1987. Lateral diffusion in an archipelago: the effect of mobile obstacles. *Biophys. J.* 52: 989-997.

Scalettar, B. A., and J. R. Abney. 1991. Molecular crowding and protein diffusion in biological membranes. *Comments Mol. Cell. Biol.* 7:79-107.

Sheetz, M. P., S. Turney, H. Qian and E. L. Elson. 1989. Nanometre-level analysis demonstrates that lipid flow does not drive membrane glycoprotein movements. *Nature.* 340:284-288.

Verkman, A. S., M. Armijo, and K. Fushimi. 1991. Construction and evaluation of a frequency-domain epifluorescence microscope for lifetime and anisotropy decay measurements in subcellular domains. *Biophys. Chem.* 40:117-125.

Wang, Y.-L., F. Lanni, P. L. McNeil, B. R. Ware, and D. L. Taylor. 1982. Mobility of cytoplasmic and membrane-associated actin in living cells. *Proc. Natl. Acad. Sci. USA.* 79:4660-4664.

Weast, R. C., Editor-in-Chief. 1986. *CRC Handbook of Chemistry and Physics.* 67th Edition. CRC Press, Boca Raton, Florida.

Wojcieszyn, J. W., R. A., Schlegel, E. S. Wu, and K. A. Jacobson. 1981. Diffusion of injected macromolecules within the cytoplasm of living cells. *Proc. Natl. Acad. Sci. USA.* 78:4407-4410.

Yoshida, T. M., T. M. Jovin and B. G. Barisas. A high-speed photomultiplier gating circuit for luminescence measurements. *Rev. Sci. Instrum.* 60(9): 2924-2928, 1989.

Zen, K., J. Biwersi, N. Periasamy and A. S. Verkman. 1992. Second messengers regulate endosomal acidification in Swiss 3T3 fibroblasts. *J. Cell Biol.* 119: 99-110.

Zhang, F., G. M. Lee and K. Jacobson. 1993. Protein lateral mobility as a reflection of membrane microstructure. *Bioessays.* 15: 579-88.

Zimmerman, S. B. and A. P. Minton. 1993. Macromolecular crowding: Biochemical, biophysical, and physiological consequences. *Ann. Rev. Biophys. Biomol. Struct.* 22: 27-65.